ELSEVIER

Nuclear Engineering and Design 189 (1999) 59–102

Nuclear Engineering and Design

The verification basis of the PM-ALPHA code

T.G. Theofanous *, W.W. Yuen, S. Angelini

Center for Risk Studies and Safety, University of California, Santa Barbara, CA 93106, USA

Received 24 August 1998; accepted 24 November 1998

Abstract

An overall verification approach for the PM-ALPHA code is presented and implemented. The approach consists of a stepwise testing procedure focused principally on the multifield aspects of the premixing phenomenon. Breakup is treated empirically, but it is shown that, through reasonable choices of the breakup parameters, consistent interpretations of existing integral premixing experiments can be obtained. The present capability is deemed adequate for bounding energetics evaluations.

1. Introduction

The purpose of this paper is to present a verification statement supporting the use of the computer code PM-ALPHA in assessing premixing of steam explosions in reactor geometries and conditions. Our specific interest is in obtaining reasonably conservative results on explosion energetics and damage potential, so as to be of use in safety analyses and for licensing purposes as well. The overall approach has been described previously (Theofanous et al., 1995). It involves a methodology (Theofanous, 1996) and a set of codes, as illustrated in Table 1. The codes are supported by respective verification documents and the approach is exemplified by the first application, as also noted in Table 1. The present paper is one (DOE/ID-10504) of this suite of documents and it should be studied in this context, as part of a whole. Most necessary in this respect is the description of the modeling approach and mathematical formulation of PM-ALPHA. They can be found in DOIE/ID-10504. In the same vein, a familiarization with 'The Study' (DOE/ID-10489) is highly recommended, prior to delving into the present details.

The structural outline of our verification approach is illustrated in Fig. 1. It provides a systematic frame for the verification task and thus a means to conclusion in this inherently open-ended endeavor. The same figure, keyed to sections and subsections, also serves to guide the reader through the wide variety of topics in this document. As the various elements in this figure are self explanatory, we defer all explanations to the respective topic. The rationale for separating into and our view of, Multifield and Breakup aspects and our emphasis on the former, derive from our modeling approach (see Appendix A of DOE/ID-10504). The Integral aspects provide a reasonable

* Corresponding author. Tel.: +1-805-8934900; fax: +1-805-8934927.

E-mail address: theo@theo.ucsb.edu (T.G. Theofanous)

0029-5493/99/$ - see front matter
PII: S0029-5493(99)00029-1

justification that this approach is consistent with available experience. However, as precious as this integral experience may be, it is and will likely remain rather limited (both in scope and measurements), hence our emphasis on the fundamentals under the Multifield aspects, for now and on the Breakup aspects in the immediate future.

Table 1
Steam explosion energetics and structural damage potential

Introductory and overall approach		The study-DOE/ID-10489 (Theofanous et al., 1995)
Topical element	Codes	Documents
Initial conditions	Special Purpose Models	In-vessel SE: DOE/ID-10505[b] Ex-vessel SE: DOE/ID-10506[a]
Premixing	PM-ALPHA	Manual: DOE/ID-10502 (Yuen and Theofanous, 1995b) Verification: DOE/ID-10504 (Theofanous et al., 1998a)
	THIRMAL	Manual: EPRITR-103417 (THIRMAL, 1993)
Propagation	ESPROSE.m	Manual: DOE/ID-10501 (Yuen and Theofanous, 1995a) Verification: DOE/ID-10503 (Theofanous et al., 1998b)
Structural response	ANACAP-3D/ABAQUS	Manual: (Hibbit et al., 1994) Verification: ANA-89-0094 (James, 1989)
Integration/application		In-vessel SE: DOE/ID-10505[b] Ex-vessel SE: DOE/ID-10506[a]

[a] The SBWR was discontinued.

[b] Actually issued as DOE/ID-10541 under the title: 'Lower Head Integrity Under In-Vessel Steam Explosion Loads', by Theofanous, T.G., Yuen, W.W., Angelini, S., Sienicki, J.J., Freeman, M., Chen, X., Salmassi, T.

All calculations in this paper have been done with the models described in Appendix A of DOE/ID-10504, implemented in the original 2D version of the code named PM-ALPHA. We now have a 3D code also, using the same models, but based on a largely different numerical scheme. This code, called PM-ALPHA-3D, has been verified at this point by comparison to PM-ALPHA in one problem, as discussed under 'Integral' aspects, code comparisons. In a further development, we also developed versions of the code with Lagrangian fuel particles, the PM-ALPHA.L and the PM-ALPHA.L-3D. These codes are also included in some aspects of the verification effort, specifically, in the interpretation of the QUEOS and FARO experiments.

2. Multifield aspects

The purpose of this step in the verification plan is to obtain unambiguous checks on the code's capability to capture 'momentum' and 'heat transfer'/'phase change' interactions in two-phase and three-phase interpenetrating continua, under well controlled and precisely known conditions. Of particular and greater interest are the internal structure of the mixing zone as compared to external (motion of outer boundary) or integral (steam flow rate) measures.

For momentum interactions in two-phase systems, we take advantage of simple analytical solutions for a single particle, obtained at the infinitely dilute limit in PM-ALPHA and of the drift flux formalism to describe slip, supported extensively by experimental data (Wallis, 1969).

For more complex situations in three-phase systems, including phase change, we have to resort to experiments and we have a whole array of such, devised specifically for this purpose. They involve particle 'clouds' poured into water and they include the original MAGICO tests and the upgraded series MAGICO-2000, designed with the help of PM-ALPHA, the more recent QUEOS tests conducted at FZK in Germany and the BILLEAU tests currently carried out at Grenoble, France.

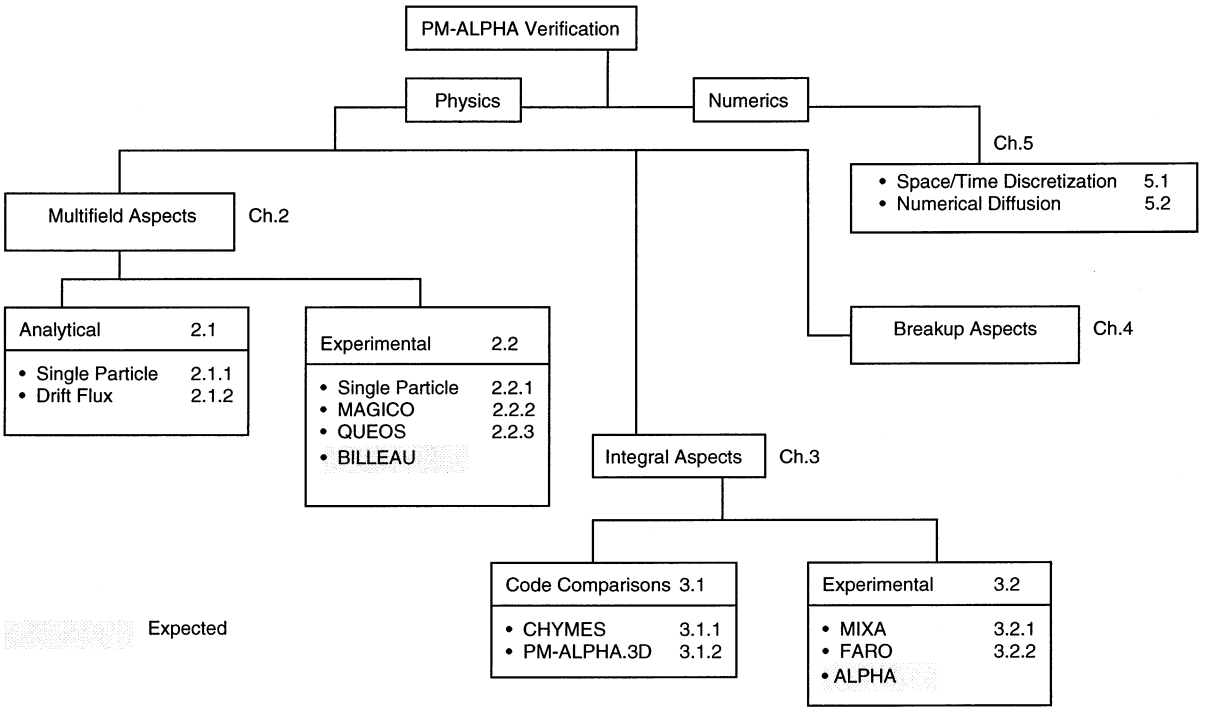

Fig. 1. Overview of the PM-ALPHA verification effort and guide through the paper.

2.1. Analytical tests

2.1.1. Single particle settling

A single particle falling in a quiescent infinite fluid reaches a steady value of the velocity when the gravitational force is balanced by the drag exerted by the fluid (terminal velocity). The gravitational force on a spherical particle in a fluid is given by:

$$F_{\text{grav}} = \frac{1}{6}\pi d^3(\rho_2 - \rho_1)g \tag{1}$$

where d is the particle diameter and ρ_1 and ρ_2 are the fluid and particle densities, respectively. Still, for a spherical particle, the drag is given by Hanratty and Bandukwala (1957):

$$F_{\text{drag}} = \frac{1}{8}C_{\text{D}}\pi d^2\rho_1 V^2 \tag{2}$$

where C_{D} is the drag coefficient and V is the relative velocity between the particle and the fluid. For a sphere in the Newton regime ($5 \times 10^2 < \text{Re} < 2 \times 10^5$), as is of interest here, the drag coefficient is constant ($C_{\text{D}} = 0.44$) and the balance between Eqs. (1) and (2) yields the following expression for the terminal velocity:

$$V_0 = 1.74\sqrt{\frac{\rho_2 - \rho_1}{\rho_1}gd} \tag{3}$$

The PM-ALPHA runs were executed by specifying a very dilute particle volume fraction (typi-

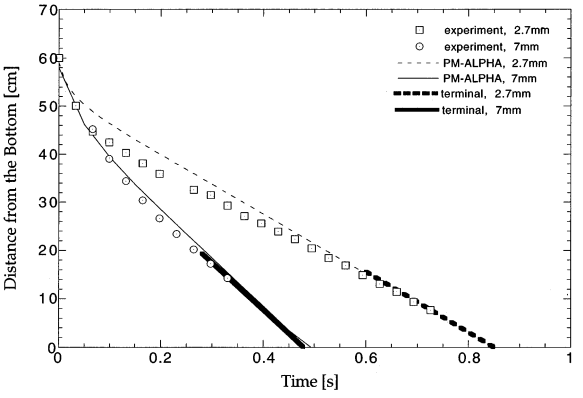

Fig. 2. Advancement of single particles in water; ZrO_2.

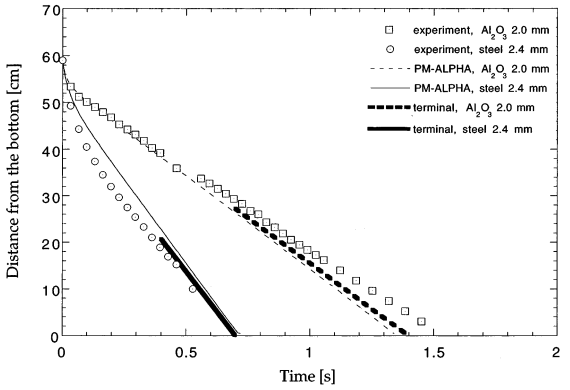

Fig. 3. Advancement of single particles in water; Al_2O_3 and steel.

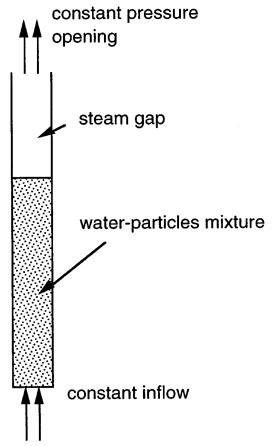

Fig. 4. Schematic of collective particle effects simulations.

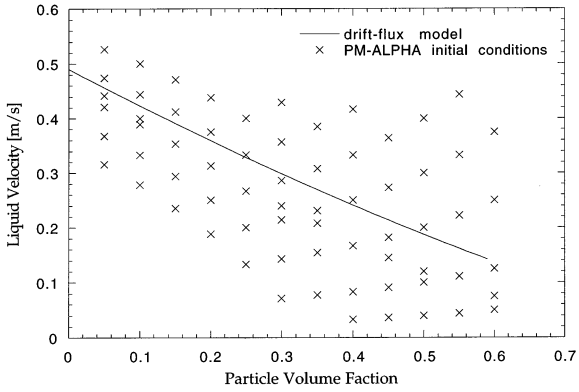

Fig. 5. Initial conditions in PM-ALPHA simulations.

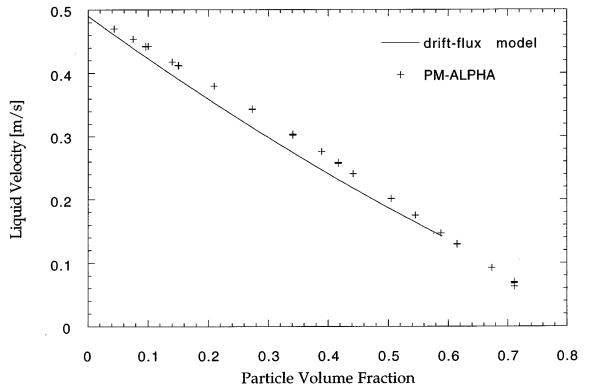

Fig. 6. Equilibrium conditions reached in PM-ALPHA simulations.

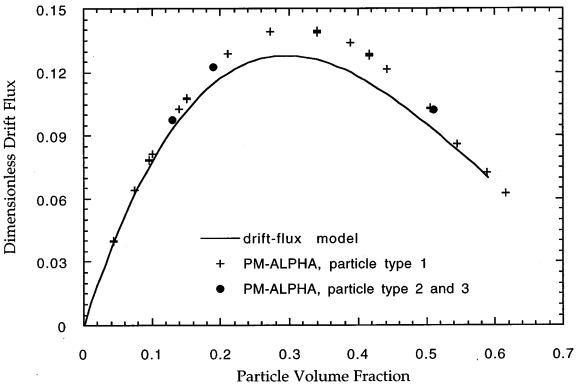

Fig. 7. Shift from initial to equilibrium conditions for representative PM-ALPHA simulations.

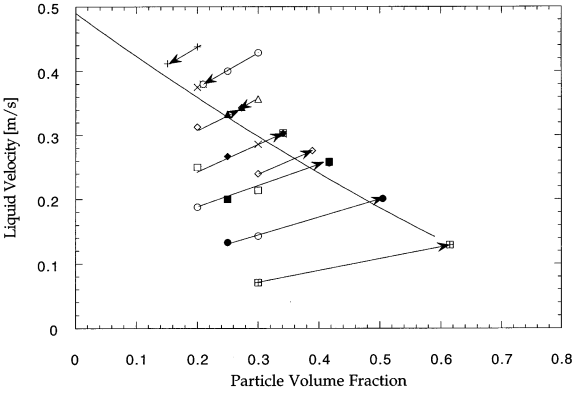

Fig. 8. PM-ALPHA simulations compared to the drift flux curve.

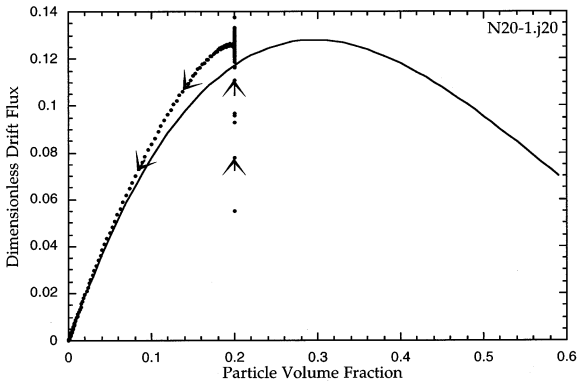

Fig. 9. Transient for glass beads, for a node in the upper part of the column; $v_0 = 15$ cm s^{-1}.

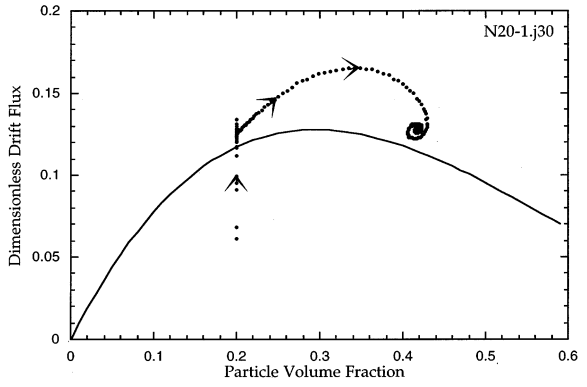

Fig. 10. Transient for glass beads, for a node in the lower part of the column; $v_0 = 15$ cm s^{-1}.

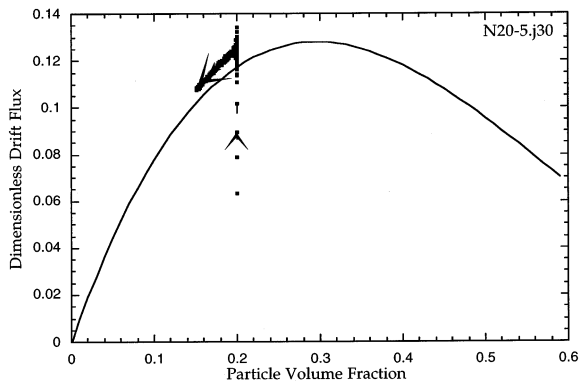

Fig. 11. Transient for glass beads, for a node in the lower part of the column; $v_0 = 35$ cm s^{-1}.

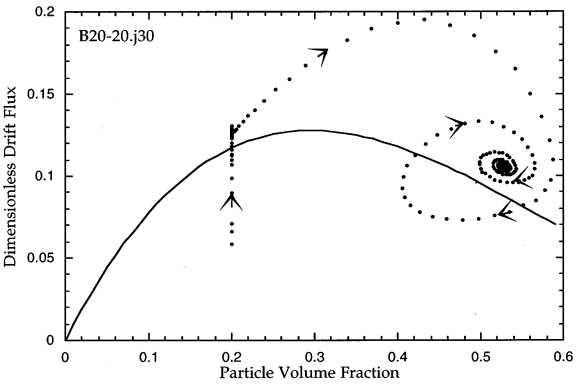

Fig. 12. Transient for steel beads, for a node in the lower part of the column $v_0 = 20$ cm s^{-1}.

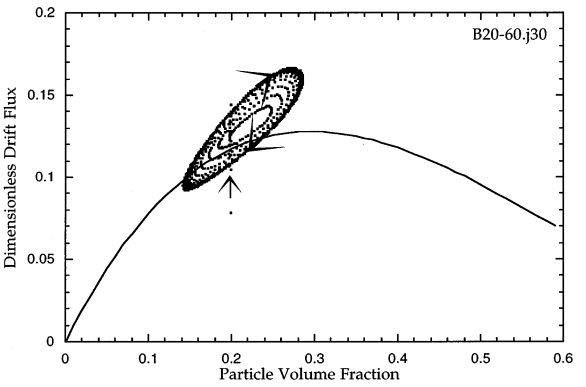

Fig. 13. Transient for steel beads, for a node in the lower part of the column; $v_0 = 60$ cm s^{-1}.

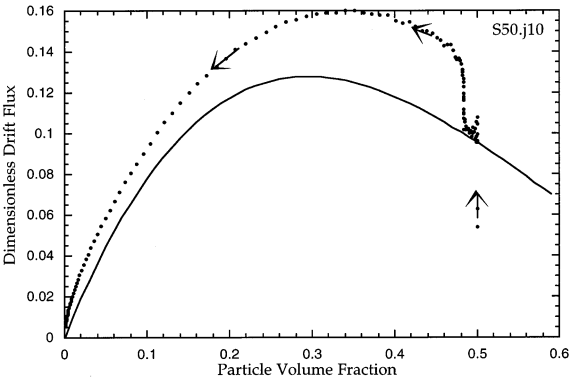

Fig. 14. Sedimentation in PM-ALPHA simulations for glass beads. Node at the top of the column.

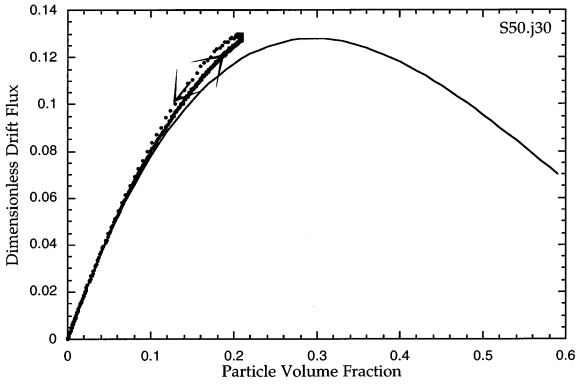

Fig. 15. Sedimentation in PM-ALPHA simulations for glass beads. Node in the middle of the column.

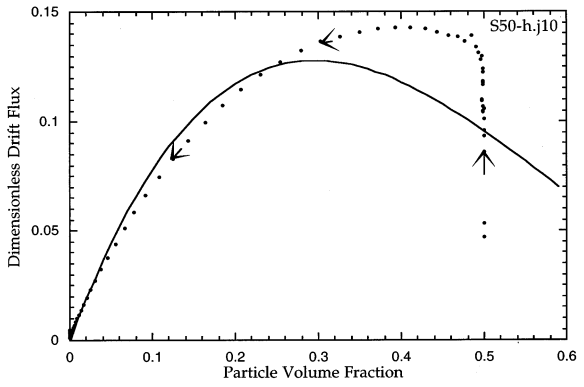

Fig. 16. Sedimentation in PM-ALPHA simulations for steel beads. Node at the top of the column.

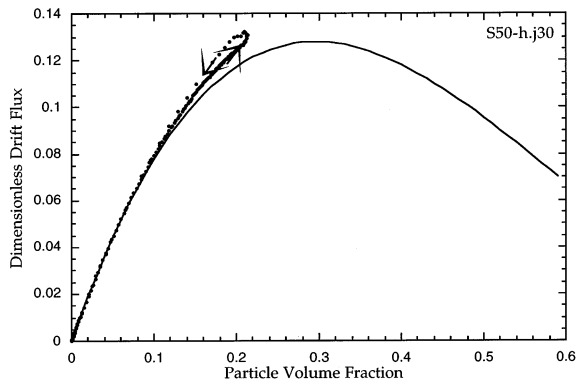

Fig. 17. Sedimentation in PM-ALPHA simulations for steel beads. Node in the middle of the column.

cally 1%) in one cell just above the free water level in a computational grid large enough to ensure that the condition of infinite medium was satisfied. An initial velocity somewhat greater than the expected terminal velocity was assigned to the particles. (Parametric tests with lower values of the initial volume fraction and different values of the initial velocity gave identical results). During the calculation, a representative particle is traced in a Lagrangian fashion. The results are shown in Figs. 2 and 3. These figures also contain experimental data which are discussed in Section 2.2.1.

2.1.2. Drift flux relations and settling of particle clouds

Consider the one-dimensional system illustrated in Fig. 4. The equilibrium condition, with the

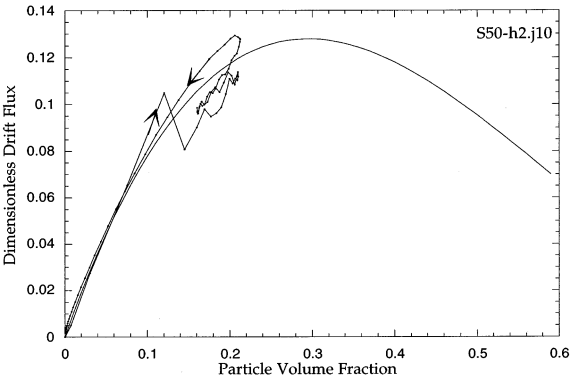

Fig. 18. Sedimentation in PM-ALPHA simulations for steel beads. Node at the top of the column. Initial particle velocity 1 m s^{-1} downward.

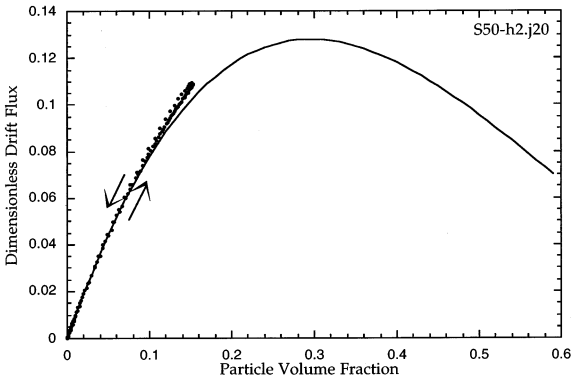

Fig. 19. Sedimentation in PM-ALPHA simulations for steel beads. Node in the lower upper part of the column. Initial particle velocity 1 m s^{-1} downward.

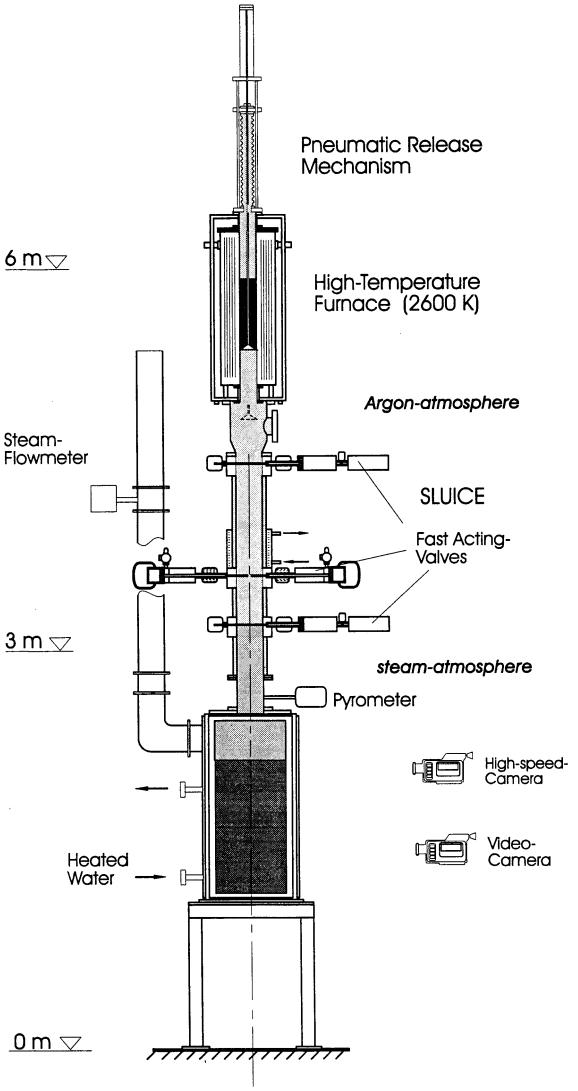

Fig. 20. Schematic of the QUEOS facility (from Meyer and Schumacher, 1996).

particles simply suspended by the flow, can be found from

$$v_1 = -\frac{J_{21}}{\alpha(1-\alpha)} \tag{4}$$

where v_1 and $(1-\alpha)$ are the liquid velocity and volume fraction in the channel and J_{21} is the drift flux. For a monodispersed system of spherical particles J_{21} is generally given by

$$\frac{J_{21}}{v_\infty} = \alpha(1-\alpha)^v \tag{5}$$

where $v = 2.39$ (for $\mathrm{Re} > 500$, i.e. Richardson and Zaki, 1954) and v_∞ is the rise (or sink here, i.e. $v_\infty < 0$) velocity of a single particle in an infinite volume of fluid. We thus obtain

$$v_1 = -(1-\alpha)^{1.39} v_\infty \tag{6}$$

or in terms of the superficial liquid velocity, J_1 (equal to the liquid velocity at the inlet, v_0)

$$J_1 = v_0 = -(1-\alpha)^{2.39} v_\infty \tag{7}$$

This can be solved for α as

$$\alpha = 1 - \left(-\frac{v_0}{v_\infty}\right)^{1/2.39} \tag{8}$$

to obtain the equilibrium particle concentration for any given value of v_0. The particle sink velocity, v_∞, is given by Eq. (3) in Section 2.1.1.

A large number of calculations were carried out to test whether PM-ALPHA embodies, through its drag laws, these results. Besides reproducing the equilibrium conditions, of interest was determining how (and in fact whether) equilibrium is approached from an initially off-equilibrium state and what the role of inertia is, not reflected in the above drift flux formulation, in these transient states. The j-number in Figs. 9–19 indicates the node number, counting from the top down.

2.1.2.1. Approach to equilibrium. Calculations were run with off-equilibrium initial conditions, as indicated in Fig. 5, with 5 mm glass particles (density 2.6 g cm^{-3}) and water in a 1.2 m long channel. The numerical model consisted of 40 (axial) nodes, the lower 34 occupied by water and particles (uniformly distributed at the specified initial concentration) and the top six occupied by steam. All components were initially at rest and the calculation commenced by imposing the water flow condition at the inlet. All calculations led to an equilibrium state, which, as depicted in Fig. 6, was actually quantitatively accurate. Fig. 7 depicts typical results of the 'shift' from the initial non-equilibrium condition to the final equilibrium. A further perspective of these results, in the form of the drift flux function, Eq. (5), is provided in Fig. 8. The PM-ALPHA values for the drift flux in

this figure were obtained from the computed equilibrium values of particle volume fractions and liquid velocities by

$$\frac{J_{21}}{v_\infty} = \alpha(1-\alpha)\frac{v_1}{v_\infty} \tag{9}$$

Further tests were carried out in the same geometry, with smaller (2 mm) and denser (7.8 g cm^{-3}) particles. These results are also shown in Fig. 8, as particles type 2 and 3, respectively.

2.1.2.2. Transient behavior. In the glass–water system runs, equilibrium was reached typically within ~ 10 s. Typical results of the transient evolution are shown for the runs with an initial concentration of 20% and an inlet velocity of 15 cm s^{-1} by the time trajectories in Figs. 9 and 10. These figures show the evolution in time of particle concentration and drift flux for a fixed node in the computational grid. Increasing the velocity to 35 cm s^{-1} yields Fig. 11. Switching from glass particles to steel (7.8 g cm^{-3}) and an inlet velocity of 20 cm s^{-1} gives the peculiar transient shown in Fig. 12. When for the latter conditions the velocity is increased to 60 cm s^{-1}, equilibrium is not reached, rather we have oscillatory behavior around the equilibrium condition as shown in Fig. 13.

2.1.2.3. Sedimentation. Another set of results is shown in Figs. 14 and 15, for a longer, closed column (3 m) and a highly non-uniform initial particle concentration. In these calculations, mimicking a sedimentation process, there were 100 axial nodes, the top seven of which, again, formed a steam gap. The top ten liquid nodes were specified to contain particles with a volume fraction of 50% and null velocity. Fig. 14 shows the transient in a node initially loaded with particles as it is slowly, by gravity, depleted. Fig. 15 shows the transient in a lower position in the grid, which sees its concentration first increase and then decrease as the particles, by gravity, flow through it. Equivalent results for heavy particles are shown in Figs. 16 and 17. An interesting demonstration of dynamics due to inertia effects can be seen in Fig. 18, obtained with the same conditions as Fig. 16 but with the particles initially in the vapor space and a downward velocity of 1 m s^{-1}. Further down in the column these inertia effects die off, as Fig. 19 shows.

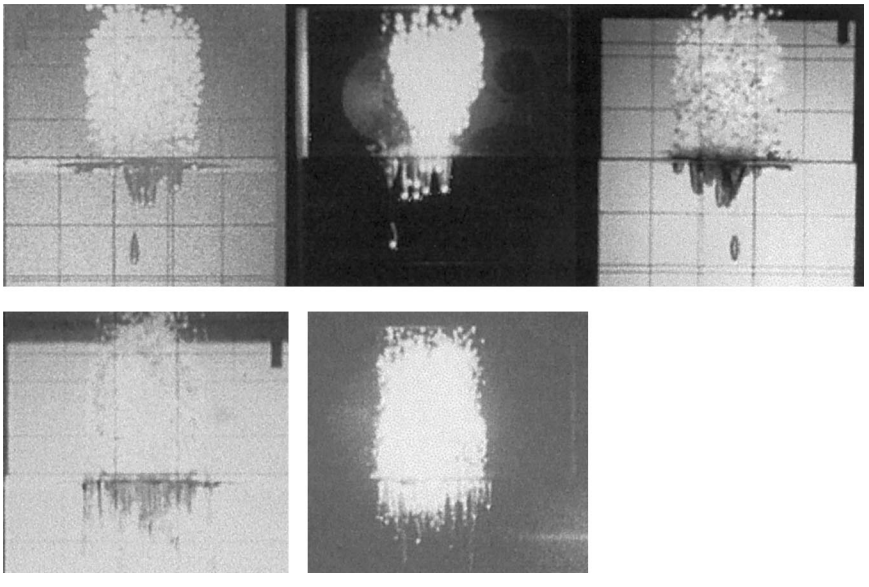

Fig. 21. Particle images for runs Q10 (top row) and Q11 (bottom row). The left and middle columns are taken with high-speed cameras from two sides 90° from each other. The far right is taken with a video camera.

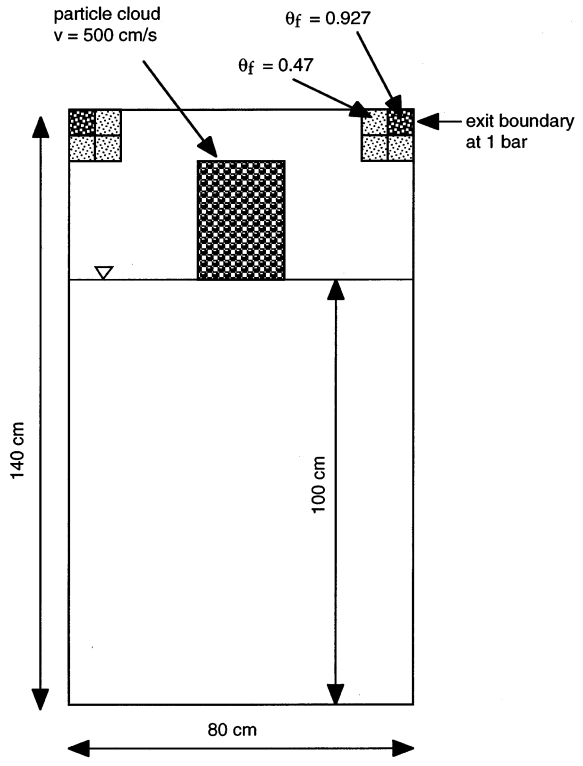

Fig. 22. The computational domain used in the PM-ALPHA simulation of the QUEOS experiments. The porous obstacles near the exit cell are to create the proper flow restriction and exit pressure drop.

2.2. Experimental tests

2.2.1. Single particle settling

The results of Section 2.1.1 were supplemented by observing the settling of single particles in the laboratory. The experimental data are shown against the predictions in Figs. 2 and 3. The measured velocity of aluminum oxide particles appears to be slightly lower than predicted. This could be due to small quantities of air (microbubbles) trapped on the relatively rough surface of this light particle.

2.2.2. The MAGICO experiments

This work spanned two experiments: the original MAGICO and the subsequent MAGICO-2000, with temperatures up to 1500°C. The results have been presented previously (Angelini et al., 1995). More recent results with more extensive use of X-rays in 2D geometries and including cold as well as hot runs, to temperatures up to 2000°C, are compared to PM-ALPHA and PM-ALPHA.L in separate papers (Angelini et al., 1997; Theofanous et al., 1998).

2.2.3. The QUEOS experiments

These experiments have become available recently (Meyer, 1996; Meyer and Schumacher, 1996); they are very similar in concept to those of MAGICO-2000 and involve similar masses of particles. The key difference is higher particle densities and concentrations (compacted cloud). Another major difference is that MAGICO characterized the internal structure of the premixture, while QUEOS provided the steaming flow rates. Both experiments measured the level swell, from which average premixture void fractions can be deduced and video images were obtained of the outside appearance and motion of the premixing zone.

The remarkable conclusion from these tests (Meyer, 1996) was that the steaming and related water depletion in the premixture, was much less than 'expected'. On the contrary, our analyses will demonstrate that these results were perfectly reasonable and consistent with PM-ALPHA predictions. Moreover, we will demonstrate that the experimental conditions created a *highly sensitive regime*, possibly useful from a fundamental perspective, but not quite relevant to the reactor conditions of interest here. To our knowledge, no other analytical interpretations of these tests are available.

The QUEOS experimental apparatus is illustrated in Fig. 20. The particulate is transferred from the furnace region to an intermediate chamber in the pipe that connects the furnace to the test vessel and then it is released to the test vessel. These operations are carried out by fast-acting valves (sliding doors). In this manner, the particulate is released, as a 'slug', from its maximum packing density of 55–65% for the Mo and ZrO_2 spheres, respectively. Some axial spreading occurs due, mainly, to the door opening time measured at ~ 40 ms. Thus, from an initial height of ~ 8 cm (for the 10 kg Mo, or 7 kg ZrO_2 tests), the cloud extends to ~ 28 cm yielding an *average*

estimated volume fraction of ~17%. This is about one order of magnitude greater than the volume fraction employed in the MAGICO experiments. Since the total particle volumes and the lateral dimensions of the pours were about the same, this implies also about an order of magnitude *shorter* clouds (and *higher* concentrations) in QUEOS as compared to MAGICO-2000. As can be deduced by comparing the QUEOS (see below) with the MAGICO-2000 (Angelini et al., 1995) results, these differences have major implications on particulate-water contact and associated vapor production and mixing dynamics.

Another key difference relative to MAGICO-2000 was the saturation status of the water pool. In the saturated MAGICO-2000 runs, true saturation over the whole pool depth was obtained, by boiling with immersion heaters at the pool bottom. In QUEOS, the pool was brought to a uniform temperature of 99.5°C by circulation through an external heater, aided by radiation lamps. The quoted uncertainty is ±0.2°C (L.

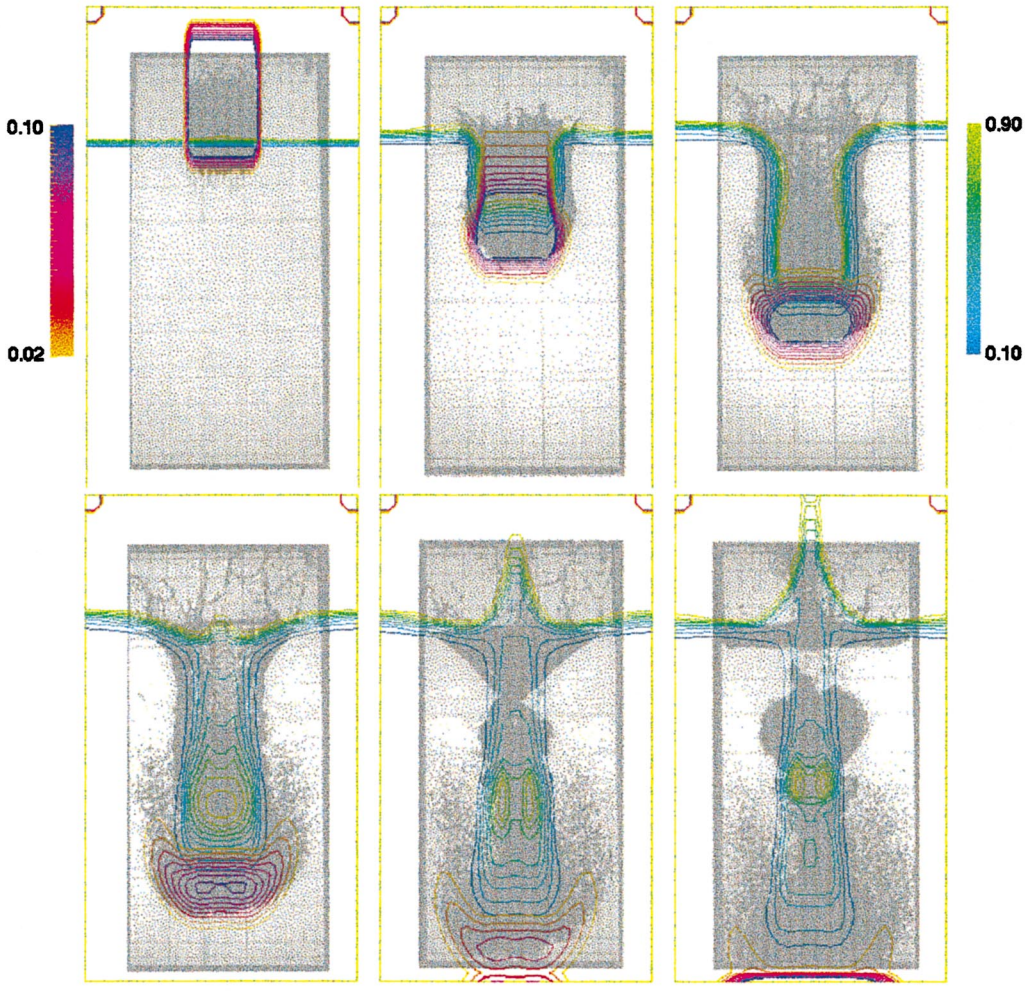

Fig. 23. Comparison of predicted against observed flow regime development in test Q8. The experimental image has been made partially transparent by computer processing, so as to allow superposition of the computed contours. Times are 0.01, 0.09, 0.17, 0.25, 0.33 and 0.41 s after first impact of the particles on the water. The color scale for the particle volume fraction is on the left; that for the void, on the right.

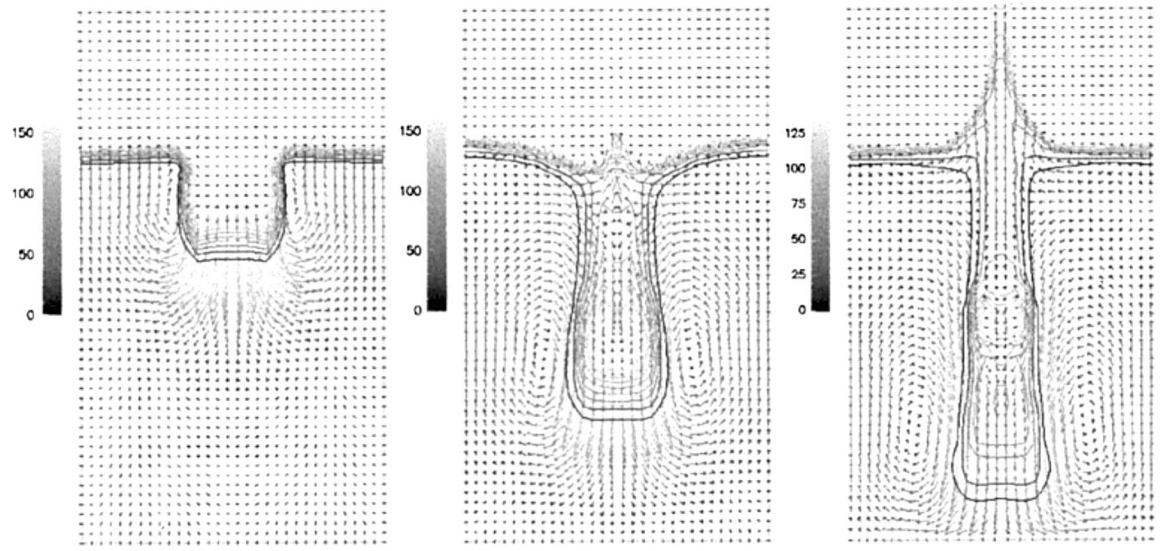

Fig. 24. Illustration of the velocity field predicted by PM-ALPHA for test Q8. Times are 0.9, 0.025 and 0.41 s after first impact of the particles on the water. Void fraction contour lines span from 10 to 90% in 10% intervals. The magnitude of the liquid fluxes (velocity times local liquid fraction) is indicated by the greyness scale (in cm s^{-1}).

Meyer, personal communication). This means that the subcooling varied from 0.5 ± 0.2°C at the pool top, to 3 ± 0.2°C at the pool bottom. Because of the compact cloud structure and its rapid descent through the pool, steaming occurred as a 'puff', with significant condensation effects in the latter portion of this descent and it is recalled that in MAGICO-2000 we found measurable effects even with a subcooling of only 3°C. As a consequence, this small, but non-negligible, subcooling creates a rather *sensitive* regime for vapor flow rates in the experiments, particularly those at the lower end of vapor production potential such as Q10 (large particles) and Q11 (small particles, but also half the volume). We believe that it would be very useful to conduct some QUEOS tests under fully saturated conditions.

It may be worth noting also that due to the release mechanism and masses involved in QUEOS the resulting particle clouds should be expected to be highly non uniform and that the internal structure has not been determined experimentally. Fortunately, the impact of non-uniformity appears (based on PM-ALPHA sensitivity studies) to be overshadowed by the shortness of the cloud, its compact, in any case, nature and the important deceleration and radial spreading suffered upon interaction with the water pool. In the calculation reported here, we used uniform clouds at the $17 \pm 2\%$ average volume fraction quoted in the report. It was obtained from cold particle pours and was found to be independent of material and particle size. We checked this value using cloud images from two hot runs (Q10 and Q11; see Fig. 21) and the results were within the specified error bounds—for Q11, a renormalization is needed, to account for the lower mass, but the volume is essentially the same (this confirms the assertion above that the particle cloud elongation for all these pours depends mainly on the door opening time). Applying the same approach for Q17 we used a volume fraction of 22.9%.

In a first approach to the interpretation of the QUEOS experiments, we selected a total of seven runs, three cold and four hot ones. The cold runs were Q5, 6 and 8 and they were chosen to include both materials (ZrO_2 and Mo) and all three particle sizes (4.2, 5 and 10 mm). The hot runs selected from the experiment report were Q10 and Q11; they included both materials (ZrO_2 and Mo) and two particle sizes (4.2 and 10 mm). They were typical of low and intermediate steaming rates

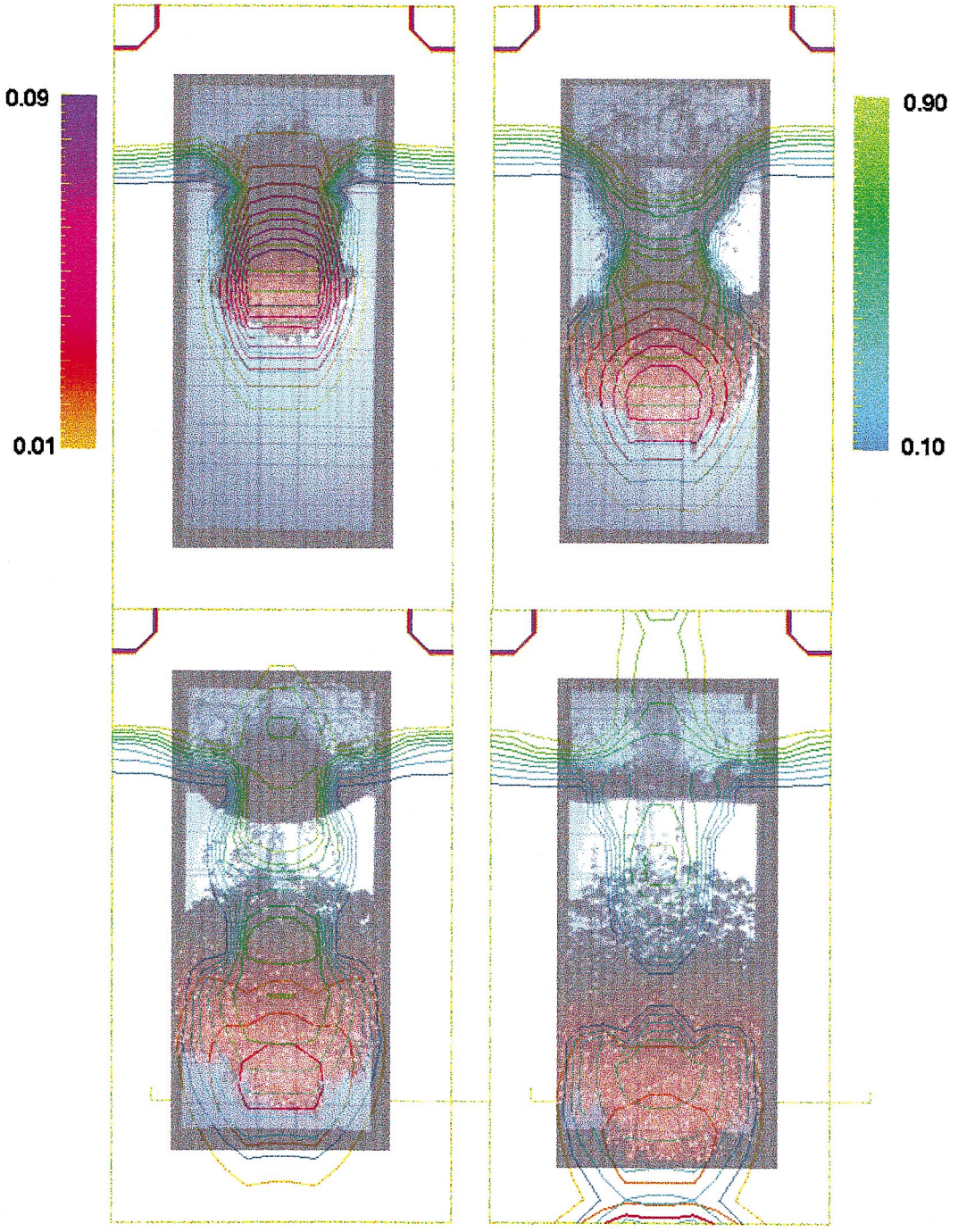

Fig. 25. Comparison of predicted against observed flow regime development in test Q10. The experimental image has been made partially transparent by computer processing, so as to allow superposition of the computed contours. Times are 0.1 and 0.2 s (top) and 0.3 and 0.4 s (bottom) after first impact of the particles on the water. The color scale for the particle volume fraction is on the left; that for the void, on the right.

over the range of experimental conditions in the report. Additional data became available more recently (Meyer, 1996) and from these we chose Q17 and 34. Q17 is the run that gave the maximum steaming among all the QUEOS experimental runs so far. The test was run with 10 kg of 4.2

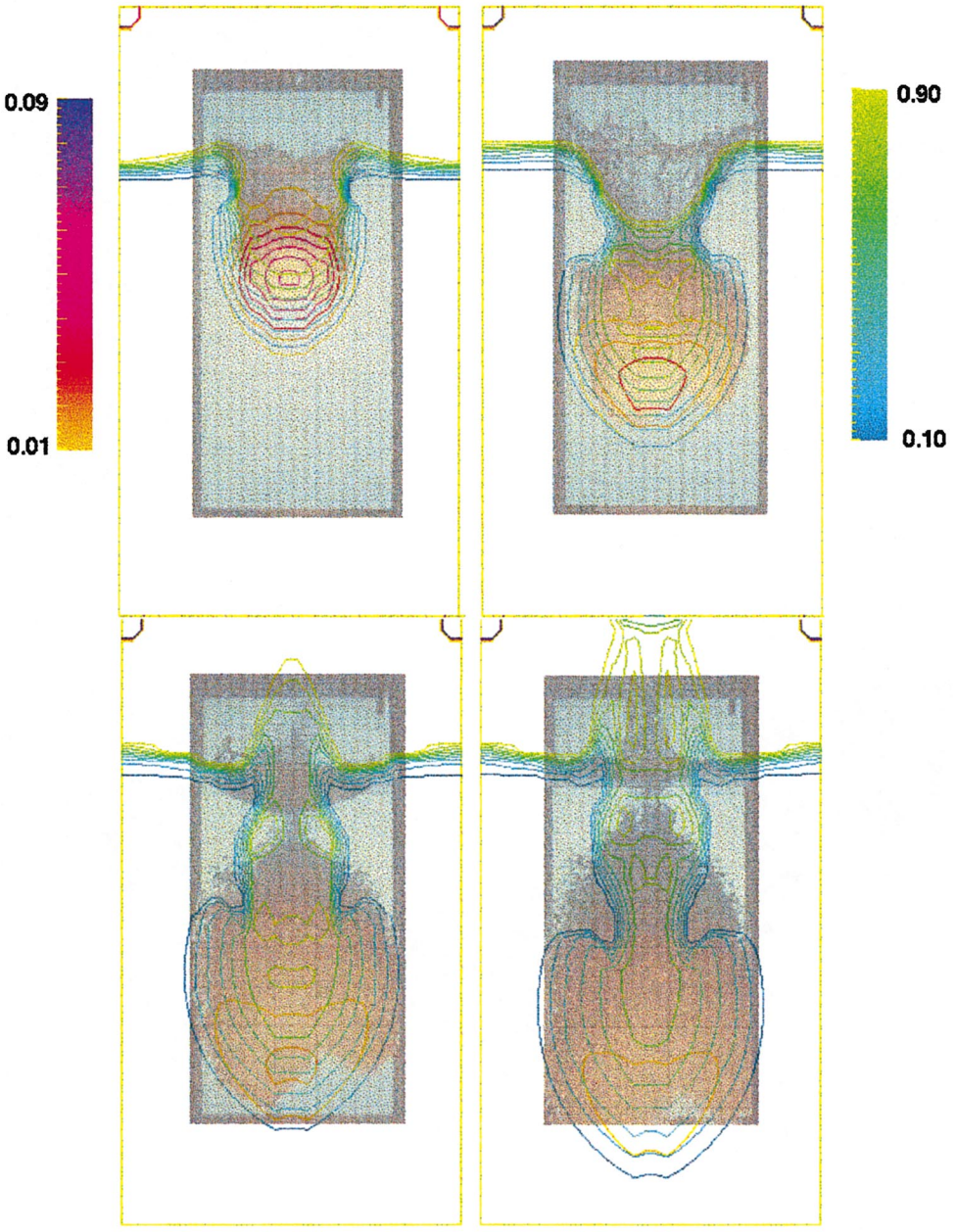

Fig. 26. Comparison of predicted against observed flow regime development in test Q11. The experimental image has been made partially transparent by computer processing, so as to allow superposition of the computed contours. Times are 0.1 and 0.2 s (top) and 0.3 and 0.4 s (bottom) after first impact of the particles on the water. The color scale for the particle volume fraction is on the left; that for the void, on the right.

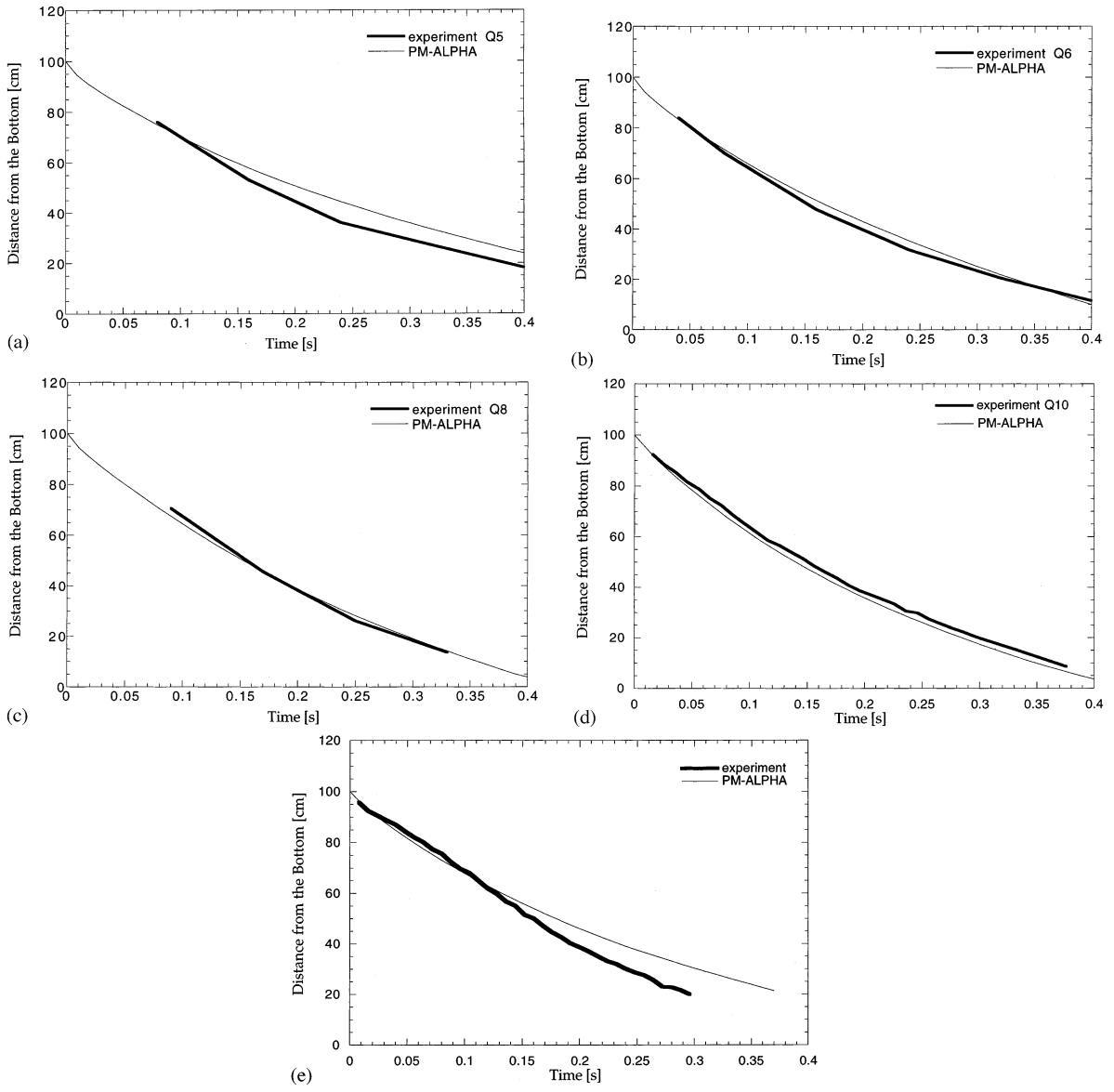

Fig. 27. (a) Comparison between PM-ALPHA predictions (Lagrangian particles) and the measured front advancement of Q5. (b) Comparison between PM-ALPHA predictions and the measured front advancement for Q6. (c) Comparison between PM-ALPHA predictions and the measured front advancement for Q8. (d) Comparison between PM-ALPHA predictions and the measured front advancement for Q10. (e) Comparison between PM-ALPHA predictions and the measured front advancement for Q11. The deviation at latter times appears to be due to front shape instability as was observed also in MAGICO-2000 runs.

mm Mo spheres at 2200 K. Q34 is a run with a long (125 cm) and narrow (10 cm diameter) pour and a larger total mass (14 kg) of 10 mm ZrO_2 spheres.

The computational domain employed is shown in Fig. 22. The QUEOS test chamber is modeled as a cylindrical volume with the same cross sectional area (80 cm in diameter). We use grid sizes,

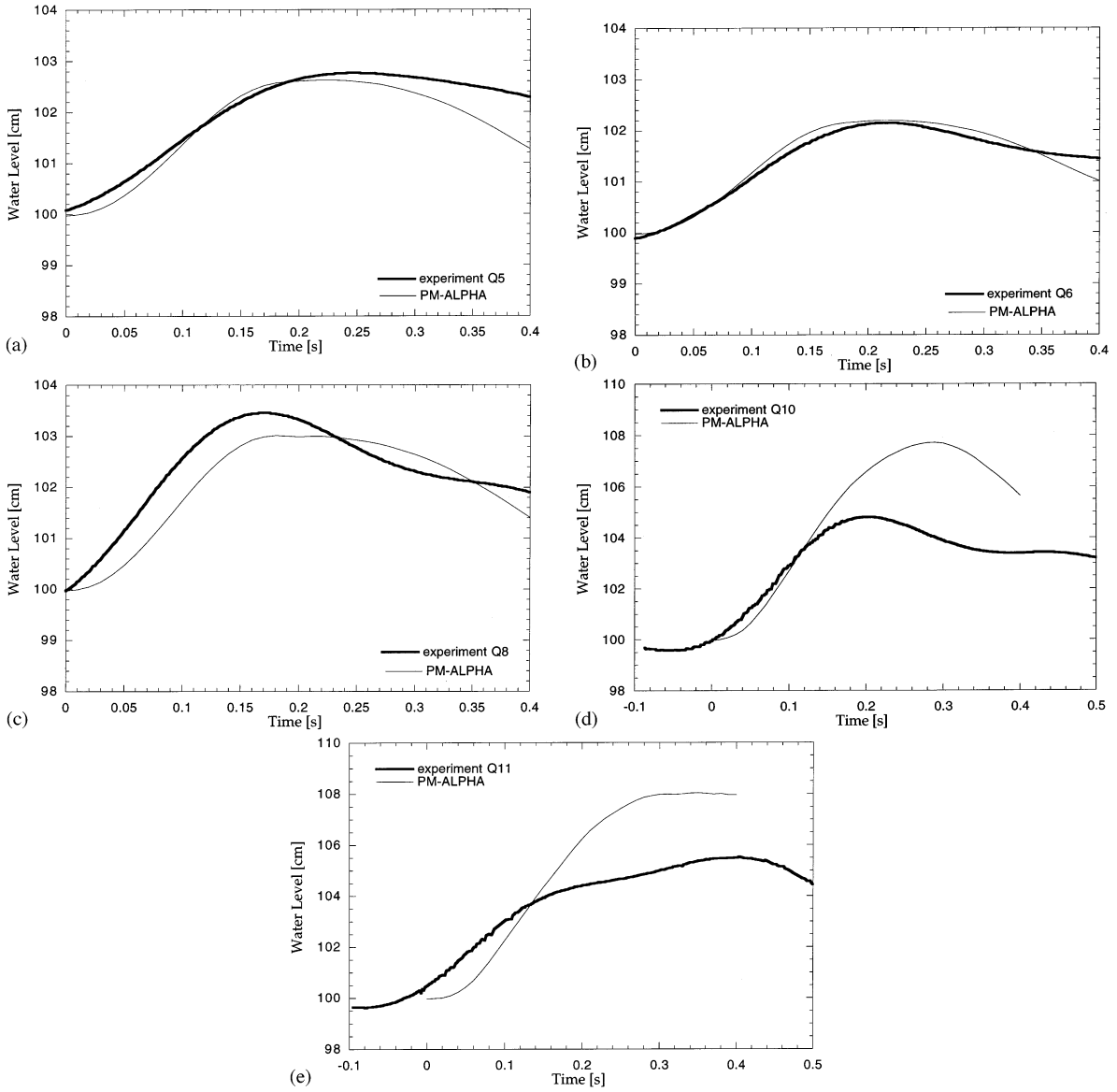

Fig. 28. (a) Comparison between PM-ALPHA predictions and the measured level swell for Q5. ($t = 0$ represents the time at which the particle clouds contact with water). The experimental trace was shifted by 100 ms, as the uncertainty in establishing the zero-time was not specified. (b) Comparison between PM-ALPHA predictions and the measured level swell for Q6. ($t = 0$ represents the time at which the particle clouds contact with water). The experimental trace was shifted by 50 ms, as the uncertainty in establishing the zero-time was not specified. (c) Comparison between PM-ALPHA predictions and the measured level swell for Q8. ($t = 0$ represents the time at which the particle clouds contact with water). The experimental trace was shifted by 60 ms, as the uncertainty in establishing the zero-time was not specified. No explanation for the instrument 'undershoot' (shown here for $0 < t < 0.06$ s) to below the steady value was provided in the experimental report. (d) Comparison between PM-ALPHA predictions and the measured level swell for Q10. ($t = 0$ represents the time at which the particle clouds contact with water). See text for explanation of the discrepancy. (e) Comparison between PM-ALPHA predictions and the measured level swell for Q11. ($t = 0$ represents the time at which the particle clouds contact with water). See text for explanation of the discrepancy.

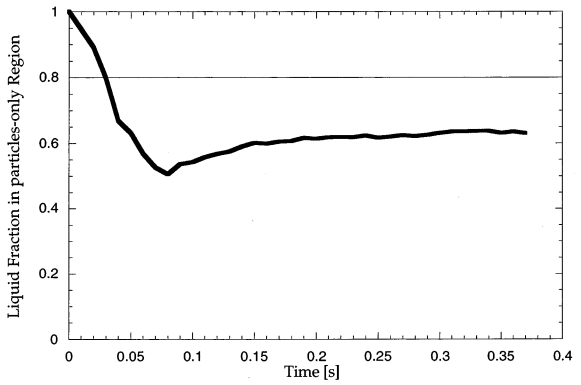

Fig. 29. The average liquid fraction, as found in the simulation of Q11, averaged over the computational cells with more than 1% volume of particles. The result is compared to a quoted value of 80% (Meyer, 1996).

$\Delta z = \Delta r$, of 2.5 or 3 cm, except for the hot runs, Q10, 17 and 34, in which we use square 5 cm grids. The code adjusts time step automatically based on stability consideration. A maximum time step of $\Delta t = 5 \times 10$ s was specified for this set of calculations. In order to interpret the pressure transient data and the induced subcooling thereof, special consideration must be given to simulate the venting mechanism in QUEOS. For Q10, this was achieved by placing obstacle cells with adiabatic, stationary particles at the exit as shown in Fig. 22. The volume fraction of the particles in the exiting cell is adjusted to match the venting area of the experiment (92 cm^2). The particle volume fraction in the adjacent cells is set to be 50% of that in the exiting cell to assure a smooth variation of particle volume fraction in that region. To simulate the effect of friction loss associated with venting, the drag coefficient between steam and particles in the obstacle cells is calibrated based on the observed data on steam flow rate versus pressure. For Q17 and 34 in which the steaming is more intense (the peak pressurization for the two tests is 0.3 and 0.1 bar, respectively), a more detailed modeling of the 5 m long vent pipe is crucial in the correct interpretation of the pressurization process. The detail of this 'venting' model is presented in the appendix.

The initial particle cloud is shown schematically in Fig. 22. The starting time of the calculation is taken to be the initial contact between the particle cloud and the water surface. The results of the computations are presented, in conjunction with the experimental data, in the following. These comparisons focus on the time frame up to 0.4 s, at which time the particles hit the pool bottom and are 'captured' by the collection cells em-

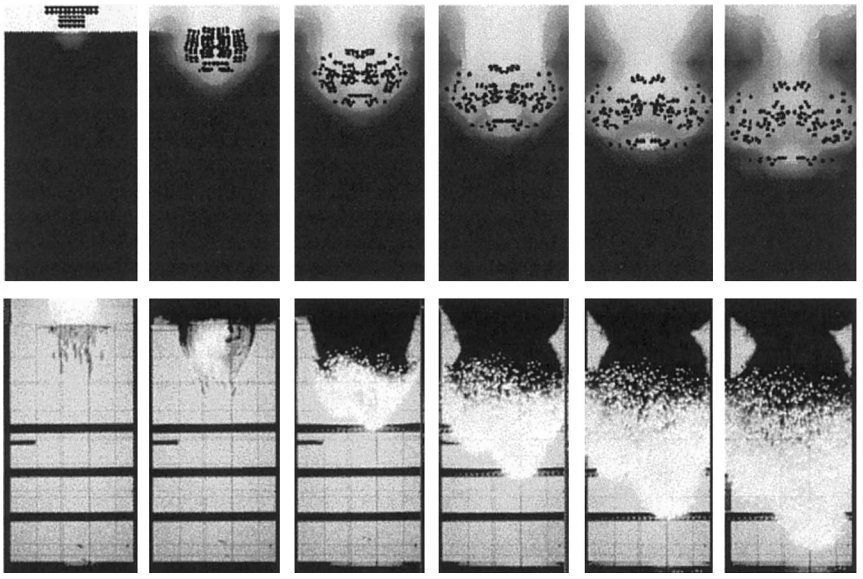

Fig. 30. Visual comparison of the PM-ALPHA.L simulation with QUEOS test Q17. Frames are at 50 ms intervals.

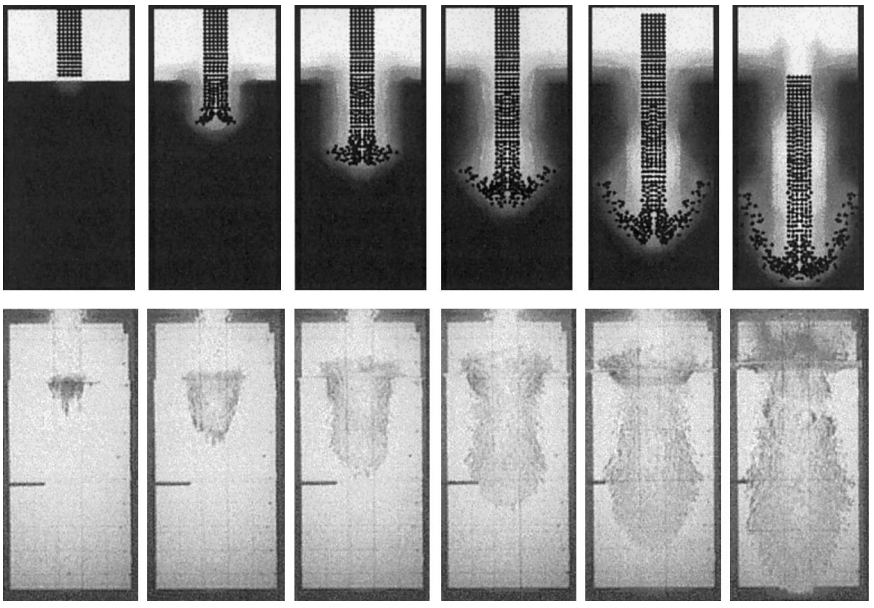

Fig. 31. Visual comparison of the PM-ALPHA.L simulation with QUEOS test Q34. Frames are at 50 ms intervals.

ployed in the experiment. (Many more results of the computations can be found in DOE/ID-10504).

First, we examine the flow regime development by superposing calculated volume fraction contours to the experimentally obtained images of the premixing zones. Such results for runs Q8, 10 and 11 are shown in Figs. 23, 25 and 26, respectively. An illustration of the velocity field in Q8 is provided in Fig. 24, to show the closing-in of the cavity created as the dense particle cloud plunges into cold water. The only observable deviation is, perhaps, a somewhat stronger 'pinching' effect in this closing-in observed in the experiment. This may be due to somewhat stronger, than calculated, circulation induced in the surrounding liquid and its potential significance is to produce a somewhat more abrupt cutoff effect in steam flow (due to condensation) in experiments with marginal steaming rates (see pressure comparisons for hot runs, below). This cavity formation behavior and closing-in had been, in fact, first predicted with PM-ALPHA and confirmed by observation in specially conducted cold runs in MAGICO-2000. Also, for the condition of the hot MAGICO-2000 runs (inlet particle volume fractions of a few percent) such cavity formation is not predicted, nor is it observed (see also Angelini et al., 1997).

More easily discernible comparisons of flow regimes can be made with respect to specific features such as front advancement using Lagrangian particles (Fig. 27) and level swell using collapsed liquid level from PM-ALPHA (Fig. 28). In Fig. 28, the experimental traces were shifted by amounts noted in the captions (50–100 ms), since uncertainty for the zero-time in these traces was

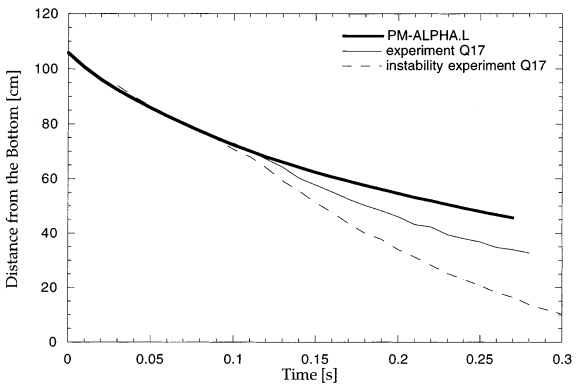

Fig. 32. Comparison of the advancing fronts for Q17.

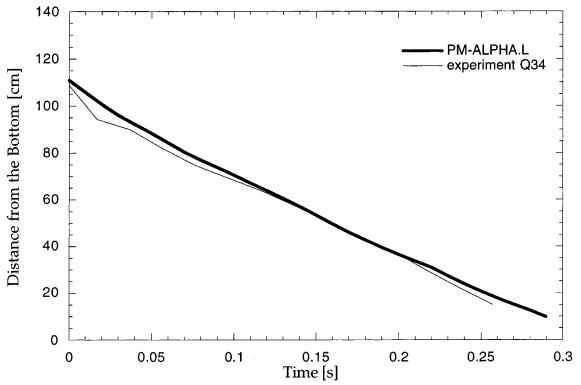

Fig. 33. Comparison of the advancing front for Q34.

not specified in the experiment records. The only significant discrepancy is observed for the hot runs Q10 and 11. This discrepancy can be explained by the 'pinching' effect noted above and associated condensation phenomena. In particular, note in Figs. 25 and 26 that between 0.2 and 0.3 s the steam cavity has closed (in the experiment) and that this corresponds well with the termination of the rapid level rise, as seen in Fig. 28d and e. In the calculation, on the other hand, as seen in Figs. 25 and 26, the condensation and closing-off of this region is delayed and as a consequence, the level continues to rise for another ~ 100 ms, creating the discrepancy. It should be emphasized, however, that such phenomena are exaggerated here due to the small, compact character of the particle clouds and the small subcooling (for large subcoolings the timing of this behavior is not very sensitive).

We also consider the degree of voiding in the premixing zone for Q11. This can be done on an overall, average, basis, based on the level swell observed and the mixing region volume, obtained from an outline of the visual image. To more specifically address void fractions in the lower part of the zone that contains the particles, one needs to consider (subtract) the apparent cavity ('funnel') seen in the visual images and this is complicated by not knowing the amount of liquid within it. Moreover, it is not possible to discern from the visual records what fraction of the total mixture volume contains particles, where the highly depleted (in water) funnel ends and what the extent is of the in-between, two-phase (steam–water) region. By assuming that the 'funnel' did not contain any water, Meyer deduced that the water content in the particle-mixing-region was $\sim 80\%$. Our PM-ALPHA result for the central

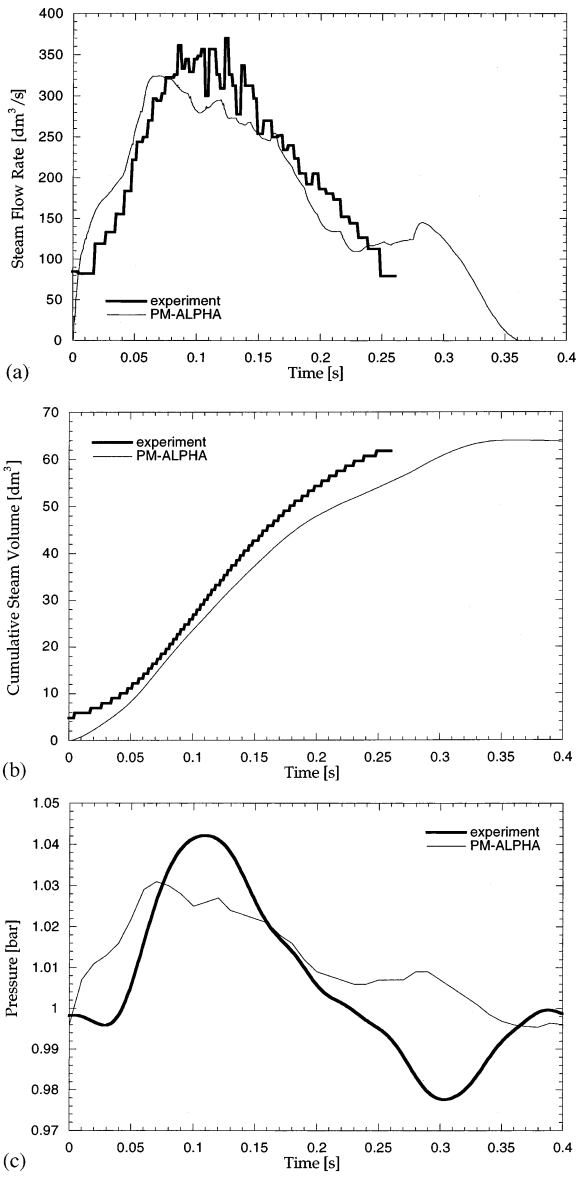

Fig. 34. (a) Comparison between PM-ALPHA predictions and the measured steam flow rate for Q10. (b) Comparison between PM-ALPHA predictions and the measured cumulative steam volume released in Q10. (c) Comparison between PM-ALPHA predictions and the measured pressure transient in the gas space for Q10.

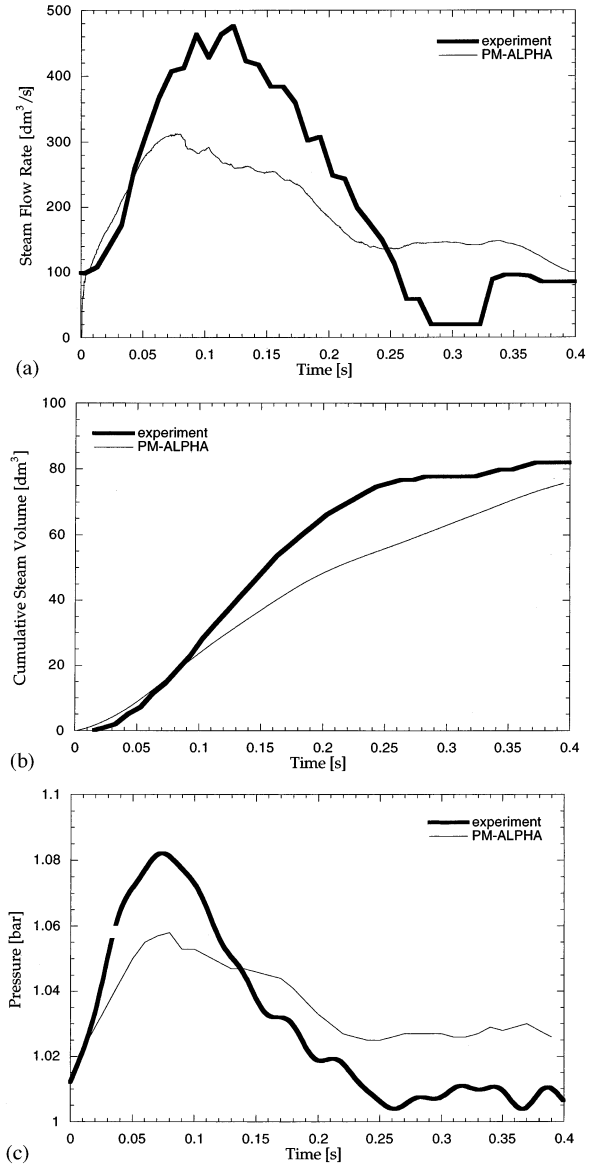

Fig. 35. (a) Comparison between PM-ALPHA predictions and the measured steam flow rate for Q11. (b) Comparison between PM-ALPHA predictions and the measured cumulative steam volume released in Q11. (c) Comparison between PM-ALPHA predictions and the measured pressure transient in the gas space for Q11.

region of the mixture, containing the main portion of the particle cloud, is shown in Fig. 29. The agreement, clearly, is not quantitative, however, it is noted that the general trend is similar in that the premixture is not highly depleted of water. Clearly, local measurements are needed to reliably assess the quantitative aspects. Such measurements have been attempted in QUEOS, but it is clear from the discussion that the data obtained are preliminary at this time.

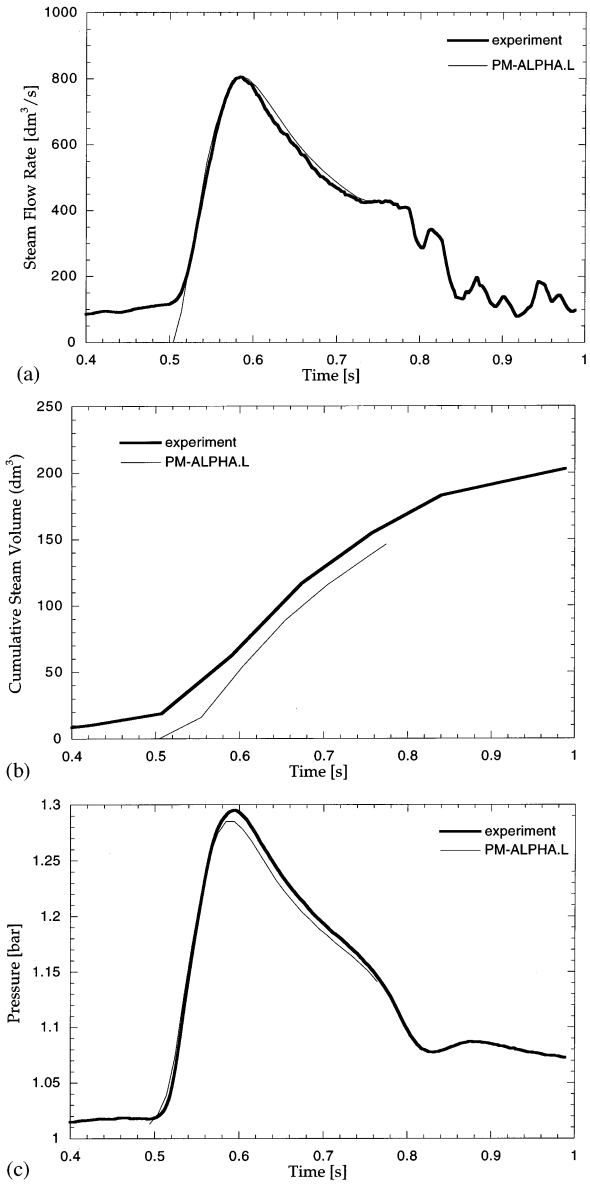

Fig. 36. (a) Comparison between PM-ALPHA predictions and measured steam flow rates for Q17. (b) Comparison between PM-ALPHA predictions and the measured cumulative steam volume released in Q17. (c) Comparison between PM-ALPHA predictions and the measured pressure transient in the gas space for Q17.

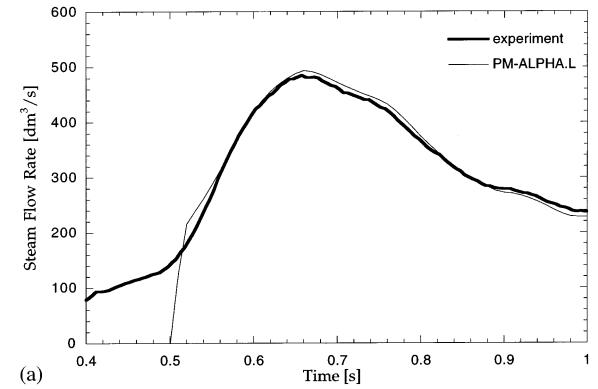

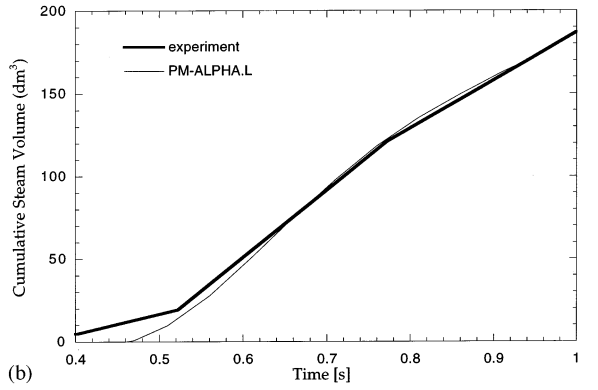

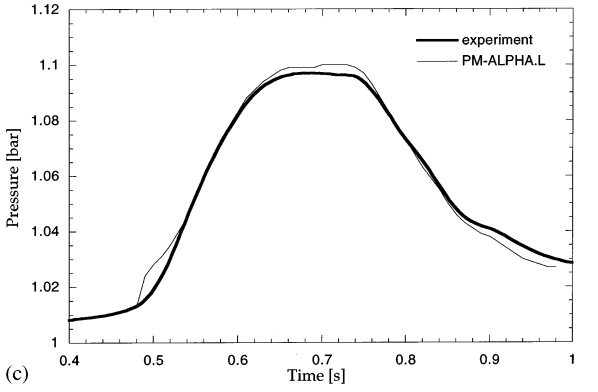

Fig. 37. (a) Comparison between PM-ALPHA predictions and measured steam flow rates for Q34. (b) Comparison between PM-ALPHA predictions and the measured cumulative steam volume released in Q34. (c) Comparison between PM-ALPHA predictions and the measured pressure transient in the gas space for Q34.

In the course of this work, PM-ALPHA.L, which includes a Lagrangian model for the fuel phase and a full turbulence-controlled heat transfer on the liquid side of the liquid/vapor interface, was developed (see DOE/ID-10504 for details of the model). Repeated analysis of Q5, 6, 8, 10 and 11 show that it produces essentially the same results as with PM-ALPHA. Since data for Q17 and 34 became available after this version of the code was ready, PM-ALPHA.L was used in the simulation of these two tests.

The results of the simulations are shown together with the visual images from the experiments in Figs. 30 and 31, for Q17 and 34, respectively. There is excellent agreement with all key features of the two interactions, the computations reflecting very well the important differences between the two runs. In particular, notice that the particle cloud shapes and dimensions are well predicted throughout the interaction (this was also observed in the Q10 results).

In Q17, the experiment exhibits a front 'breakup' and a faster penetration, similar to what had been seen already in MAGICO (see DOE/ID-10504). These 'instabilities' appear to be peculiar to short, dense clouds and occur even under cold conditions. While interesting on fundamental grounds, we expect them to play a very limited role in assessing the premixing of steam explosions.

The quantitative comparison of the advancing fronts of the interaction zones for these two runs are shown in Figs. 32 and 33. The agreement for Q34 is typical of cases where the front remains coherent. The disagreement observed in Q17 is also typical of cases that develop instabilities, such as short, compact clouds.

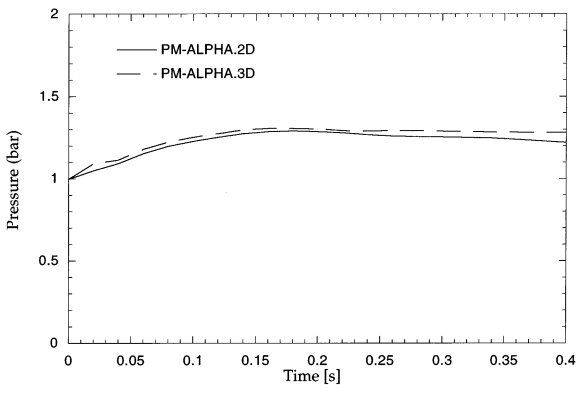

Fig. 38. Comparison between the PM-ALPHA-3D and PM-ALPHA-2D prediction of the pressure transient.

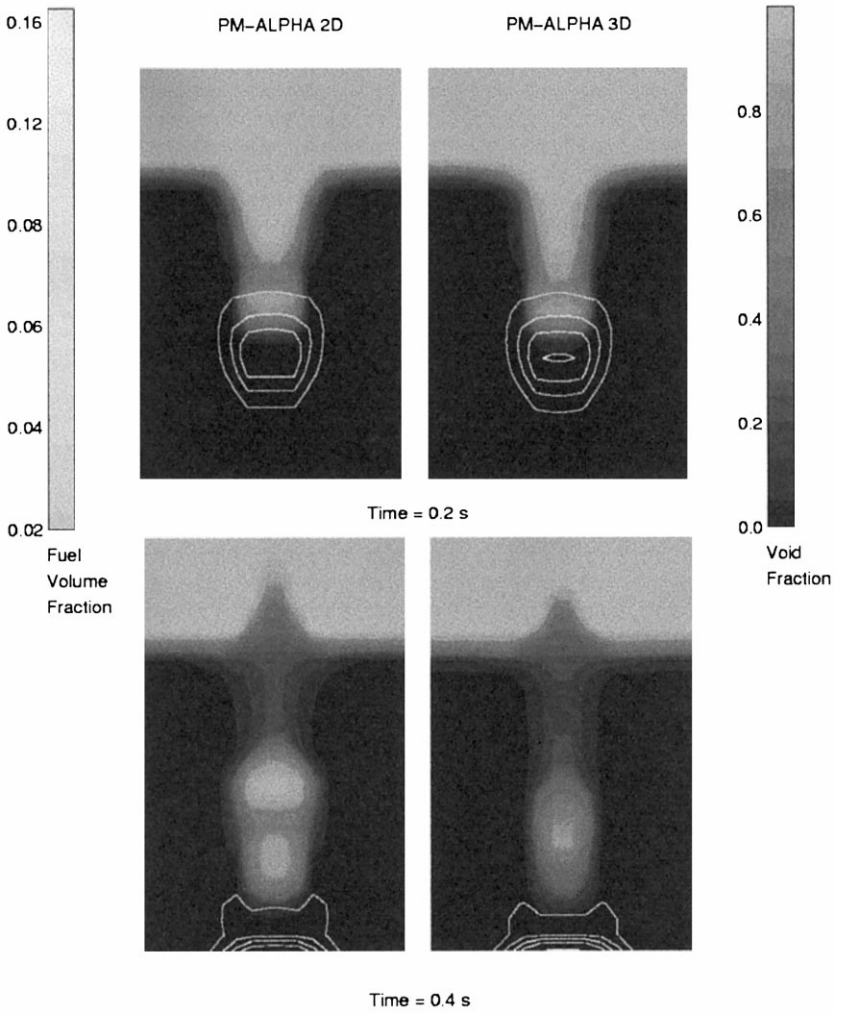

Fig. 39. Comparison between the PM-ALPHA-3D and the PM-ALPHA-2D prediction of the premixing behavior.

Integral aspects of the thermal interaction were obtained experimentally by measuring steam flow rates exiting the vent pipe and pressure transients in the enclosed gas space above the pool. Related comparisons with PM-ALPHA results, for the four hot runs, are presented in Figs. 34–37. These figures include also the integrated volumes of steam, so as to obtain a more direct perspective on the magnitude of the interaction. We thus determine total volumes of about 60, 80, 200 and 180 ℓ for runs Q10, 11, 17 and 34, respectively. We can then clearly see that Q10 and 11 produced minimal interactions and this also can be seen by the slight increase in pressure observed in the gas volume. Indeed, a quantity of 60 or 80 ℓ is only a very small fraction of this gas space—it has a volume of ~ 200 ℓ. The pressure comparisons should be examined in this context and for the trailing portion of the traces the *sensitivity of condensation* under such conditions, as noted above, should be included in the consideration.

As shown in Figs. 36 and 37a, there is a nearly steady steam flow of ~ 100 ℓ s^{-1} prior to the contact of particles with water, occurring at ~ 0.5 s. This flow appears to initiate rather suddenly, ~ 100 ms earlier (these first 100 ms are not shown

in the figure) and it can be seen that it is very reproducible. Simple estimates of the heating and expansion of the steam/air mixture in the freeboard volume, or the radiative boiling at the pool surface (actually seen in the videos), indicate that neither is of sufficient magnitude to provide an explanation. Another possibility is that this flow is due to the highly superheated steam and Argon, trapped in the intermediate vessel and vented together with the cloud. Unfortunately, this cannot be evaluated, because the pressure was apparently vented prior to opening the doors, but the data are not shown to a sufficient resolution for this special purpose. The experimenters did not discuss this flow and most importantly, we cannot know whether it persists during the interaction itself. Thus, we cannot do much about this now, except to keep in mind this 'additional' flow as we look at the comparison of PM-ALPHA predictions with the experimental data for Q17 and 34.

In general, the interpretation of Q17 is quite satisfying. The calculation captures successfully both the qualitative and quantitative behavior of the pressure and flow transients. The interpretation of Q34 is not as good, but this has to be tempered by the question of the spurious flow raised above. Moreover, as such interactions become milder and milder, the scales magnify greatly as in Q34 and they become subject to slight extraneous effects as well as sensitivities.

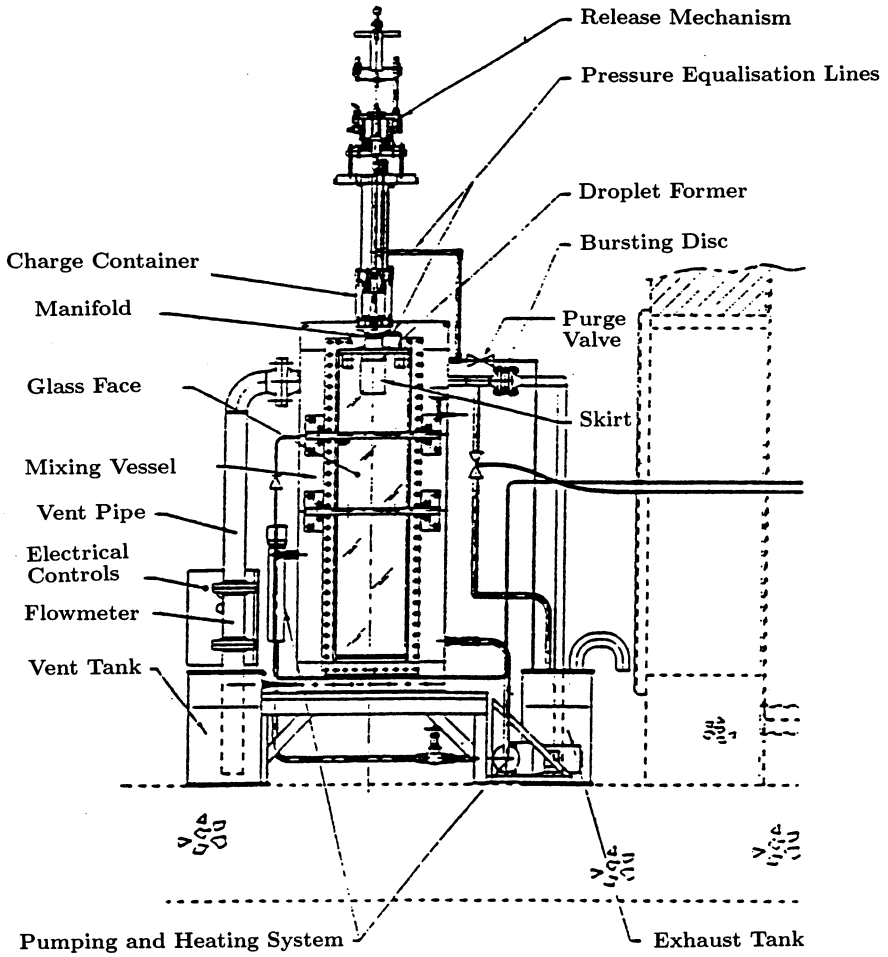

Fig. 40. Schematic of the MIXA facility (from Denham et al., 1992).

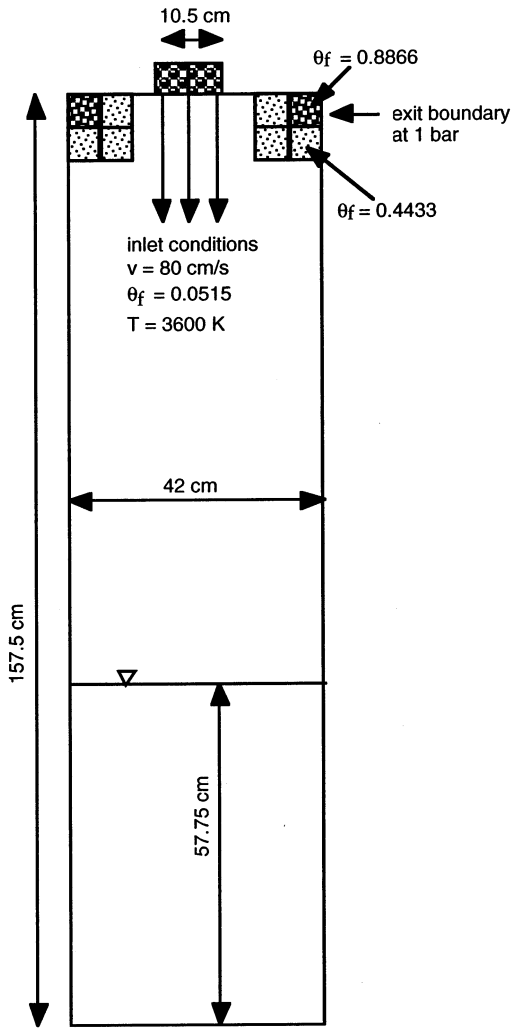

Fig. 41. The computational domain used in the MIXA06 simulations.

It is hoped that from the above the reader will deduce the highly sensitive nature of the hot QUEOS runs available at this time and will share our perspectives, expressed at the beginning of this section, that these data, while interesting from a fundamental point of view, are not quite relevant to the fitness-of-purpose needed here. It is expected that these sensitivities will be to some extent alleviated by the larger masses currently employed in QUEOS. It is also recommended that fully saturated pools be included in the test matrix, as well as subcoolings larger than merely a few degrees. Further, as indicated in the appendix and the analysis of Q17 and 34, the whole venting mechanism of the QUEOS facility must be reexamined and perhaps redesigned, if the sensitive mechanisms of condensation under the small pressurization-induced sub-cooling are to be further pursued.

3. Integral aspects

3.1. Code comparisons

3.1.1. Comparison with CHYMES

About 3 years ago PM-ALPHA and CHYMES were compared directly in two sequential papers in the open literature (Fletcher, 1992, 1995; Theofanous and Yuen, 1993—see Appendix 5 of DOE/ID-10489). The conclusion was that, once the two codes were made to address the same problem, the comparisons, even at the details of mixture zone composition, were excellent.

3.1.2. Comparison with PM-ALPHA-3D

As noted above, the PM-ALPHA-3D code was recently developed and it involves a different numerical scheme from that in PM-ALPHA. The basic solver is the same as that used in ESPROSE.m-3D and it has been verified by comparison to ESPROSE.m, as discussed in DOE/ID10503. Here, we present a further numerical test by comparing the 2D versus the 3D versions of the premixing code. As a test problem we chose a 17% volume fraction cloud of 4.2 mm particles at 2000°C and a saturated water pool in a 2D Cartesian geometry. The grid size was 5 cm (a total of 8×28 grids) and the time step 2×10^{-5} s. We have a closed air gap, so that the enclosure can pressurize with time. The results obtained with the two codes are compared in Fig. 38 for the pressure transients and in Fig. 39 for the detailed evolution of the mixture zones. The overall behavior is very similar. The 2D result generates slightly more steam and there is a slight difference in the 1% void fraction contour at $t = 0.3$ and 0.4 s. We expect this to be caused by small differences in numerical diffusion, which certainly exist due to the different numerical schemes.

3.2. Experimental tests

In this section we consider premixing experiments with the hot material being in the molten state and hence subject to breakup in the course of the interaction. Available integral tests of this type include the MIXA tests which were run with urania (20% Mo) at ~ 3600 K and the FARO tests run with UO_2 melts at ~ 3300 K. Besides the unknown, variable length scales of the melt during the interaction, these tests are also interesting in requiring a non-local radiation transport formulation—the absorption lengths in water are 3 and 5 cm at 3000 and 3600 K, respectively and this is further complicated by the presence of variably voided regions (see Appendix A of DOE/ID-10504).

3.2.1. The MIXA experiments

The MIXA experiments were run in the UK in conjunction with the CHYMES code development and validation effort (Denham et al., 1992; Fletcher and Denham, 1993). They involved the pouring of kg-quantities of thermitically generated UO_2 melts (containing $\sim 20\%$ of Molybdenum) at 3600 K, into near-saturated water pools. The experimental apparatus is schematically illustrated in Fig. 40. The 'droplet former' shown in

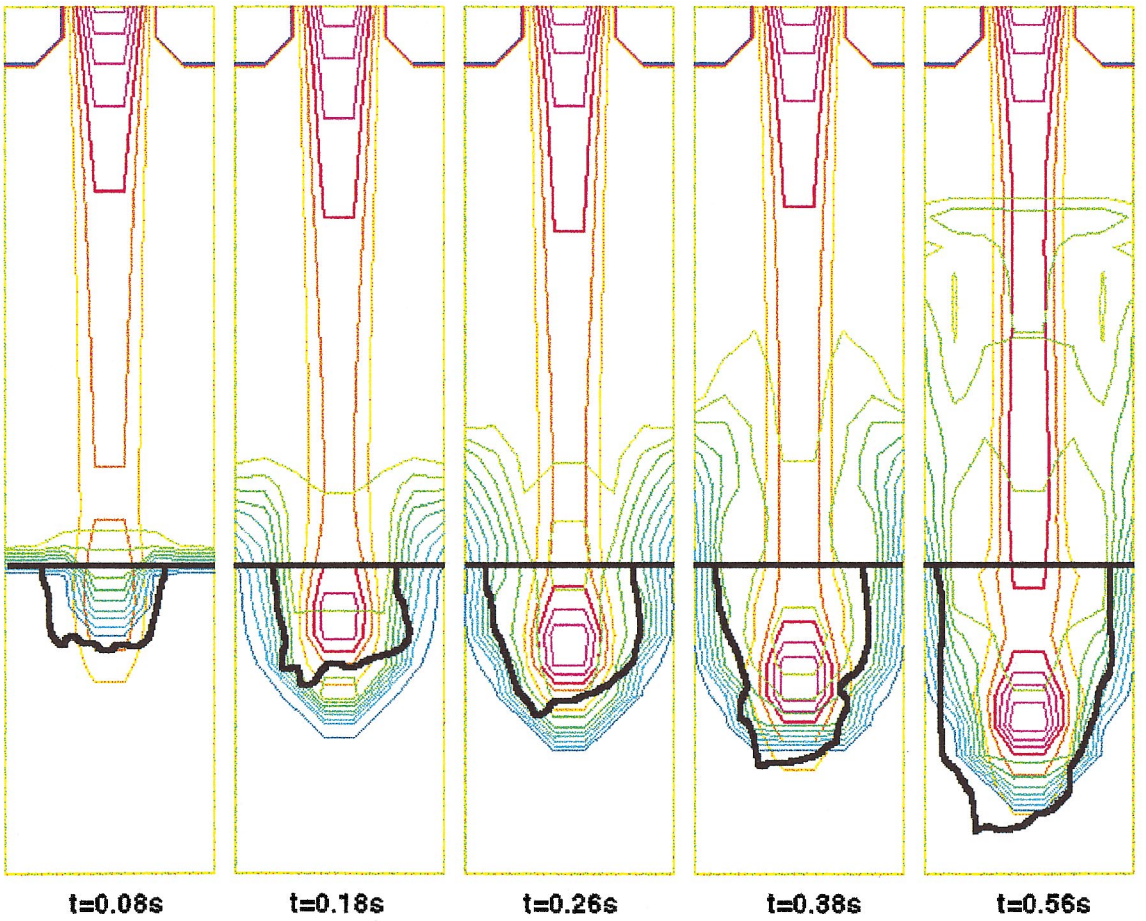

Fig. 42. Comparison of predicted against observed flow regime development in MIXA06. The experimental contour (black line) corresponds to the location of the luminous melt. The straight black line represents the initial water level. Void fraction (blue tones) span from 10 to 90%, in 10% intervals. Melt contours (red tones) span from 0.5 to 4.5%, in 0.5% intervals.

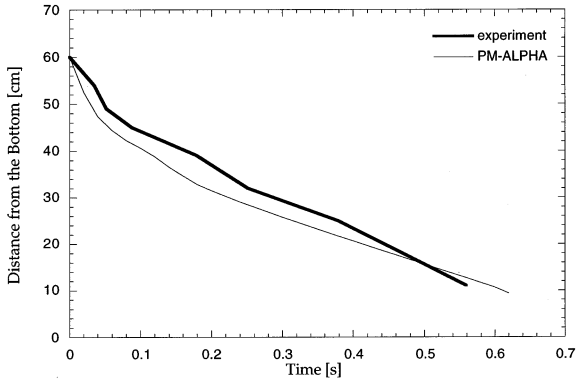

Fig. 43. Comparison between experiment and simulation of the front advancement.

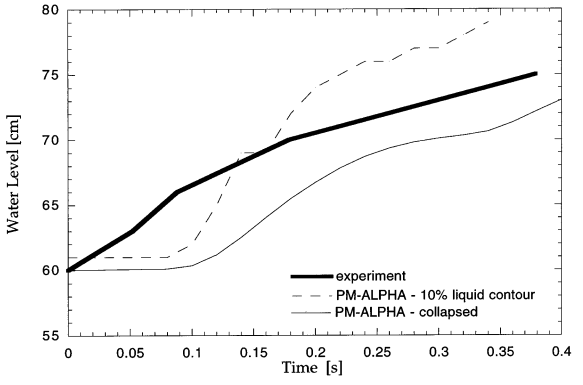

Fig. 44. Comparison between experiment and simulation of the water level swell.

the figure consisted of a graphite grid and was found to break up the melt stream into droplets of approximately 6 mm diameter. Besides visual images of the interaction, pressurization and steam flow rate data (in the vent pipe) were obtained. Of the several published tests, the MIXA06 seems to have been the most completely documented. It also included the longest skirt (see Fig. 40) that helped streamline the droplet flow vertically downwards. This test was, therefore, selected for simulation here using PM-ALPHA. It involved a 3 kg melt pour and the water pool was within 1 K from saturation. The melt release time for all the tests was nominally quoted to be in the range of 1–1.5 s, but the 1 s value appears to be appropriate for MIXA06.

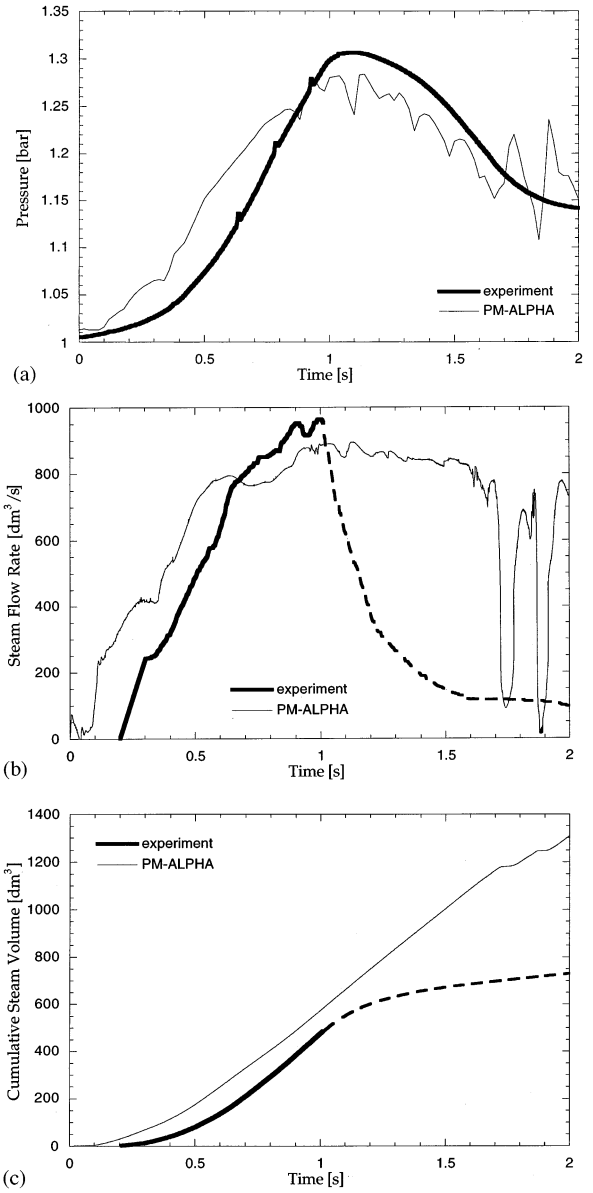

Fig. 45. Pressure, flow rate and steam volume in the simulation of MIXA06, base case: void fraction limit for breakup 85%, minimum particle size = 1.2 mm. The experimental flow rate and steam volume data have unknown uncertainty in the time base (personal communication, Turland, 1996). Also, according to the same reference, the flow rates beyond 1 s (dotted line) are not reliable (potential entrained water interference with instruments).

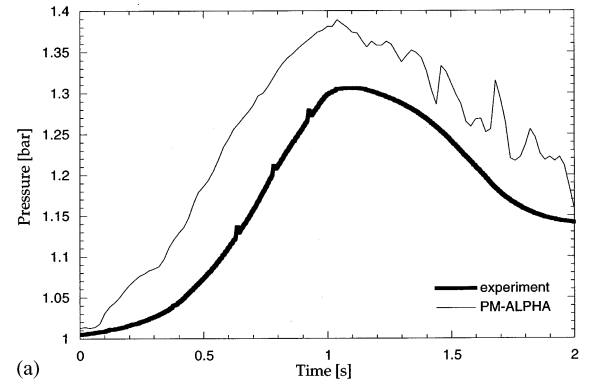

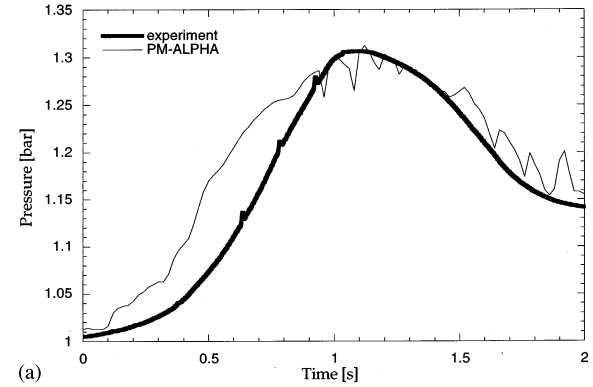

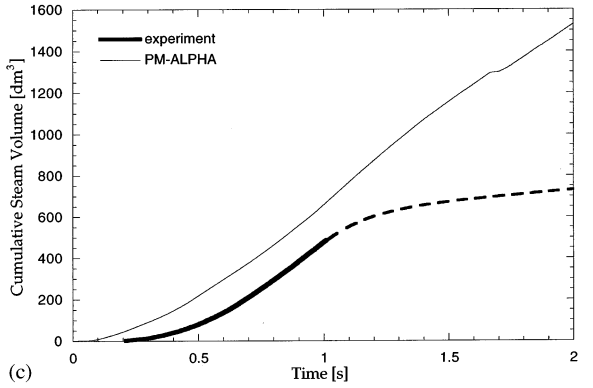

Fig. 46. Variation of the base case, with void fraction limit of 85% and minimum particle size of 1 mm.

The computational domain is shown in Fig. 41. The square-section vessel is replaced by a circular-section vessel with the same cross sectional area. We use a grid of 4×30 cells, each cell being 5.25×5.25 cm in size (confirmatory calculations with a still more refined grid are underway) with an initial steam gap of 99.75 cm (versus the experimental value of 100 cm), a water level of 57.75 cm (versus the experimental value of 60 cm) and a melt pour diameter of 10.5 cm (versus the experimental value for the pour side of 12 cm). The melt inlet rate is set at 3 kg s^{-1} with an initial melt droplet size of 6 mm. As in QUEOS, we need to model the restriction of the vent line in the experimental facility. This is accomplished by

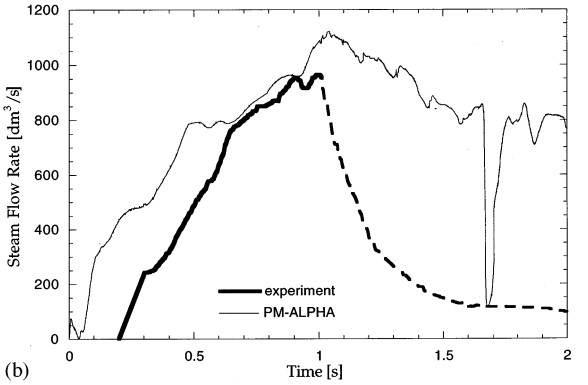

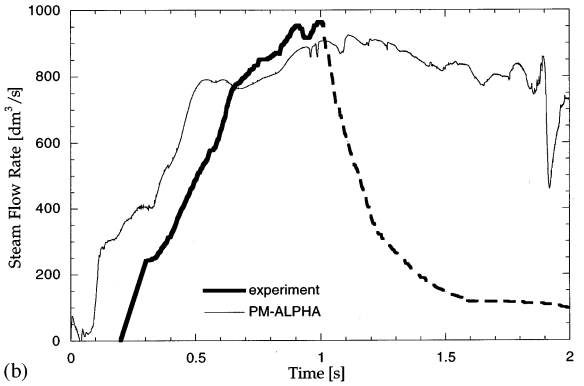

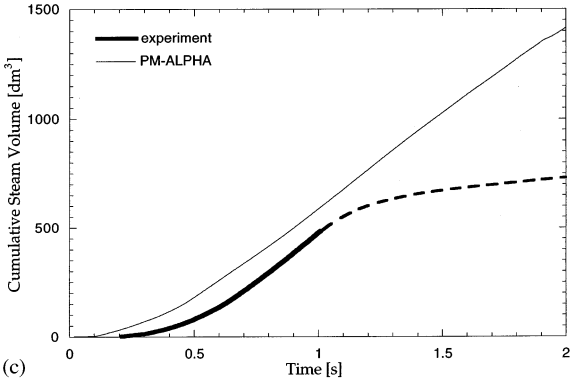

Fig. 47. Variation of the base case, with void fraction limit of 83% and minimum particle size of 1 mm.

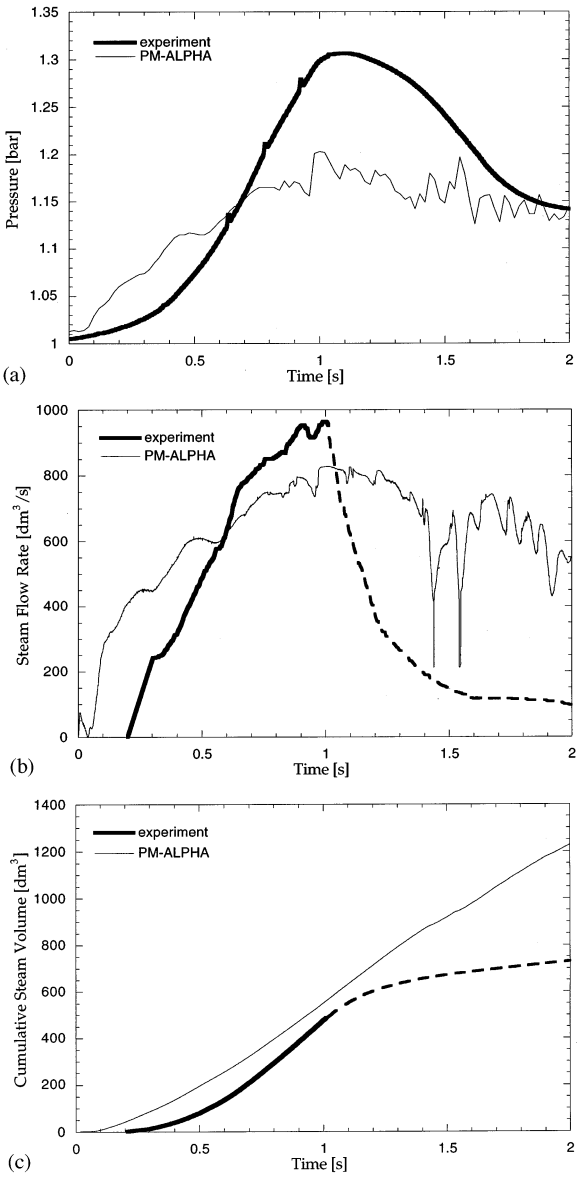

Fig. 48. Variation of the base case, with void fraction limit of 80% and minimum particle size of 1 mm.

placing cells with a specified porosity and drag coefficient to match the vent area and pressure drop characteristic in the experiment. We found the effect of the subcooling to be negligible. Time zero in the results shown below corresponds to the time the cloud front hit the water surface.

In the simulations, breakup was characterized by a β-value of 20 (see Appendix A of DOE/ID10504), a breakup cutoff void fraction of 85% (for voids above this value breakup is not allowed) and a minimum particle size of 1.2 mm. Sensitivities to the latter two parameters were determined by including combinations for cutoff values of 80 and 83% and for a minimum particle size of 1 mm.

The flow regime comparisons with the experimental data are shown in Fig. 42. The more quantitative features of the interaction such as advancement of the melt front and of the two-phase level swell, are shown in Figs. 43 and 44, respectively. The data were obtained from Fletcher and Denham, (1993).

Pressure transients, steam flow rates and cumulative steam volumes vented are shown in Fig. 45 and for variations of the breakup parameters in Figs. 46–48. The sensitivity is remarkable and provides useful perspectives on the inherent limitations of taking a predictive approach on the details of such problems.

3.2.2. The FARO experiments

In the FARO experiment prototypic corium melts in quantities of over 100 kg are released into near-saturated water pools at high ambient pressure ($\sim$ 50 bar). A schematic of the experimental facility is shown in Fig. 49 (Magallon and Leva, 1996). The interaction vessel is closed and the principal data obtained are the pressure transient in it, the level swell, water and steam temperatures and the resulting debris collected at the bottom of the vessel at the end of the experiment.

Two FARO tests (L-06 and 08) were conducted with relatively small quantities of melt (20 kg) and a shallow pool (about 1 m deep). The PM-ALPHAs interpretation of one of these experiments (L-06) has been presented elsewhere (Angelini et al., 1993). L-08 is a similar test. In one of two large scale tests (L-11), the melt contained zirconium and its exothermic reaction with water vapor was identified as an important mechanism affecting the pressurization (Magallon and Hohmann, 1995). Since the current version of PM-ALPHA does not have a chemical reaction model, the interpretation of L-11 is out of the scope of this paper. The present effort is thus focused on the two large scale tests, L-14 and 19.

The geometry of the computational domain used in the simulation is shown in Fig. 50 and the gas space is taken to include all volumes available for expansion. Note that by incorporating this volume the free space above the inlet nozzle is distorted and, therefore, level swells beyond ~2 s may be distorted too. The melt release position relative to the water level is represented by model-

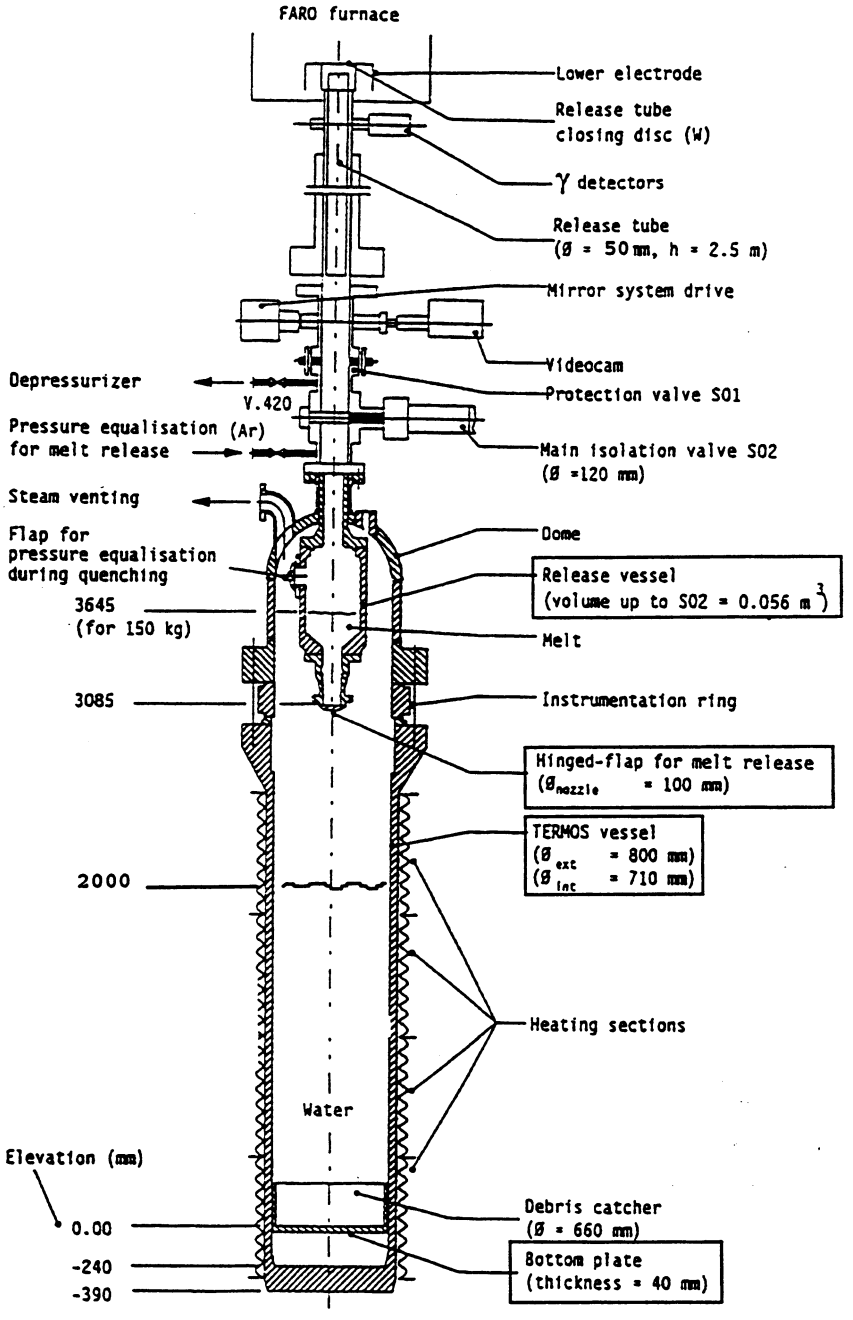

Fig. 49. Schematic of the FARO test facility (from Magallon and Leva, 1996).

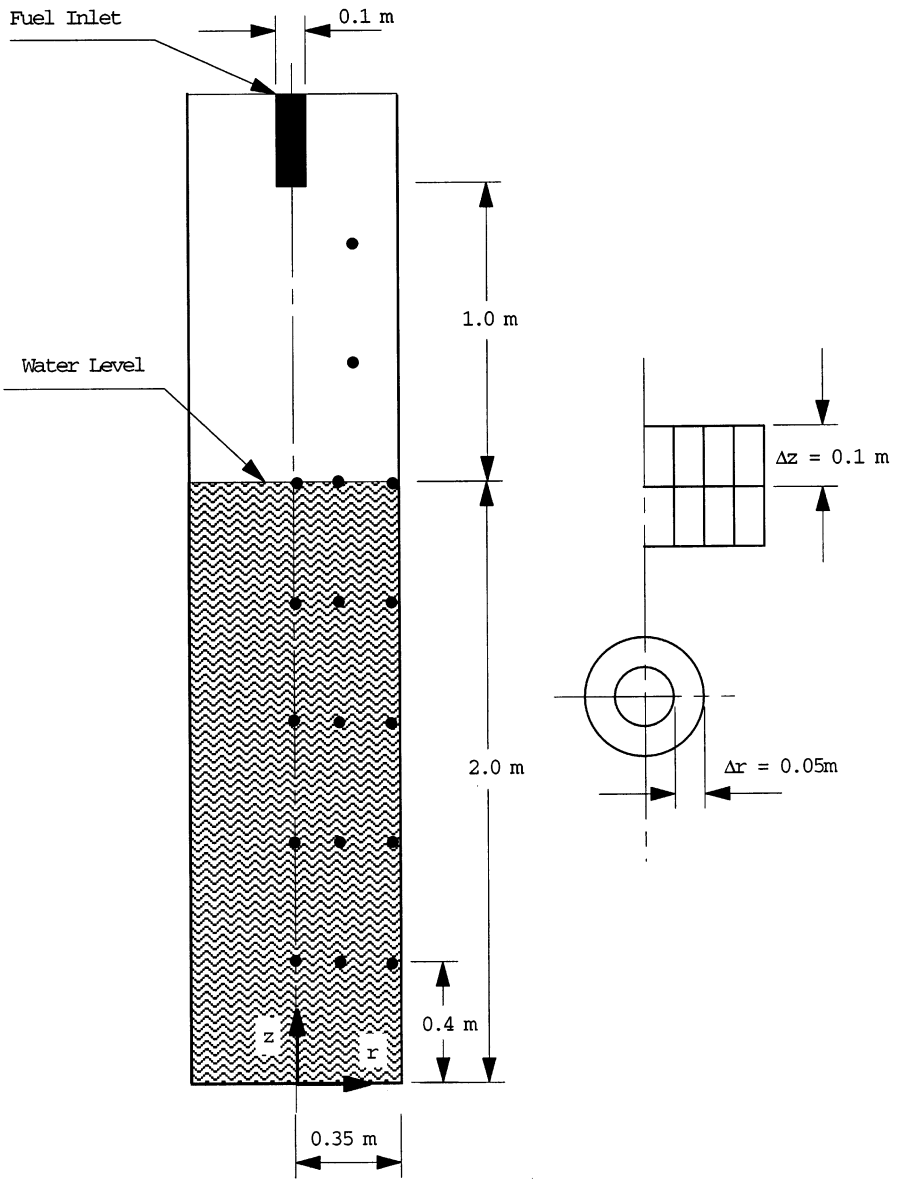

Fig. 50. The computational domain and discretization used in PM-ALPHA (axisymmetric, 2D) to simulate FARO test L-14. Also shown are the thermocouple positions at which comparisons with data are made.

ing an inlet from an interior obstacle. Calculations are carried out with a grid size of $\Delta r = 5$ cm, $\Delta z = 10$ cm and a maximum time step of $\Delta t = 1 \times 10^{-4}$ s. The actual time step is adjusted automatically by the code based on stability considerations. The code, PM-ALPHA.L, is used in the interpretation.

For L-14, an initial length scale of 4 cm (the nozzle diameter is 10 cm, but the shear reduced to ~ 5 cm during the fall in the vapor phase) is specified at the melt inlet and it is subjected to breakup using a β-value of 40. Results with $\beta = 20$ are also presented to show the sensitivity of the interpretation to the breakup parameter. For L-

19, it becomes necessary to use a considerably smaller breakup parameter ($\beta = 20$), that is faster breakup, as well as a smaller initial melt length scale (1 cm). These are appropriate trends, as the twice-as-long travel through the steam space (2 as compared to 1 m) would be expected to allow some additional breakup prior to contact with the water and a faster breakup following this contact. More specifically, in L-14, the melt arrives at the pool surface with 4 m s^{-1}, as compared to 2.8 m s^{-1} for L-19. The results are summarized in Figs. 51–60.

The calculated melt front advancement in the two experiments is compared to the experimental data (deduced from failed thermocouple reading along the centerline string) in Fig. 51. The agreement is excellent. Also note in Fig. 51 the 'suspension' of the portion of the melt at the tail end of the release, it being much stronger for L-19 characterized with smaller length scales.

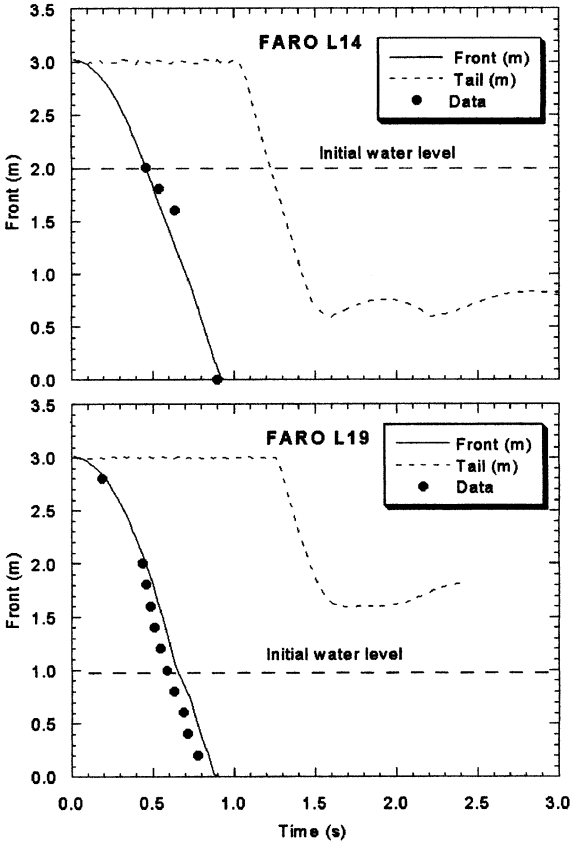

Fig. 51. Comparison between the calculated melt front advancement and experimental data for FARO L-14 and 19.

The mixing regimes for the two runs are shown in Fig. 52a,b. We observe a rather slender vapor 'chimney' penetrating to nearly the middle of the pool (~ 1 m), which is followed by a 'fainter' chimney-like two-phase structure ($\alpha \sim 40\%$) to the pool bottom. Both of these chimneys are seen to close behind the melt, at ~ 1.4 s. For the remainder of the time the rather large pool (2 m deep) is seen to be more like a slug, driven from below, as the interaction proceeds at the pool bottom. Ultimately, this is seen to develop up, along the container walls (1.6–2.3 s). Strong boiling and condensation processes are evident throughout. In L-19, on the other hand, the vapor chimney is seen to penetrate all the way to the pool bottom and to be much stronger (smaller particle length scale, faster breakup), dominating the behavior all the way to the end of the calculation (~ 2.3–2.4 s) where the interaction is seen to settle back down. That is, here the flow regime is reversed, with liquid flowing up, along the walls.

The pressure histories are shown in Fig. 53 and the effect of some parameter variations is indicated in Fig. 54. Note that in L-14 the pre-contact pressure rise (radiation heating of steam) is small and it is predicted well. In L-19, the effect is stronger, but it is underpredicted. This is because of the approximate treatment of radiation reflected from the walls in the cylindrical geometry. Accounting for this under-prediction would bring both calculations into good agreement with the pressure rise portion in L-19. For L-14, the $\beta = 20$ calculation again matches the pressure rise portion quite well. In both runs the timing of the pressure turning over (termination of the intense interaction) is seen to be predicted very well (all four cases), but the amplitude seems to be somewhat overpredicted for the parameters that yield the best prediction of the fast-rising portion ($\beta =$ 20 in L-14 and $d = 0.5$ cm in L-19). This may well be due to overpredicting the boiling-condensation balance in the extremely complex regime of the interaction at the vessel bottom. In any case, in the spirit in which such 'simulations' are made at this time, we believe that the comparisons are adequate, especially in light of the overall consis-

tency as discussed in the other paragraphs of this section. It should be noted that the effect of hydrogen production as reported (Magallon and Leva, 1996) for test L-14 (0.18–0.29 kg) on the overall pressure rise is quite small. Based on the predicted final steam temperature (~ 600 K), for example, the contribution of hydrogen to the total pressure is about 2.8–4.5 bar, which is insignificant compared to the total pressure rise.

The level swell comparisons are shown in Fig. 55 and are seen to be quite good. The energy partitions are depicted in Fig. 56 and these are consistent with deductions made from the data on the overall heat transfer by the experimenters. Specifically, in L-19, the total heat loss from the fuel at the end of 2 s was estimated to be 88.2 MJ

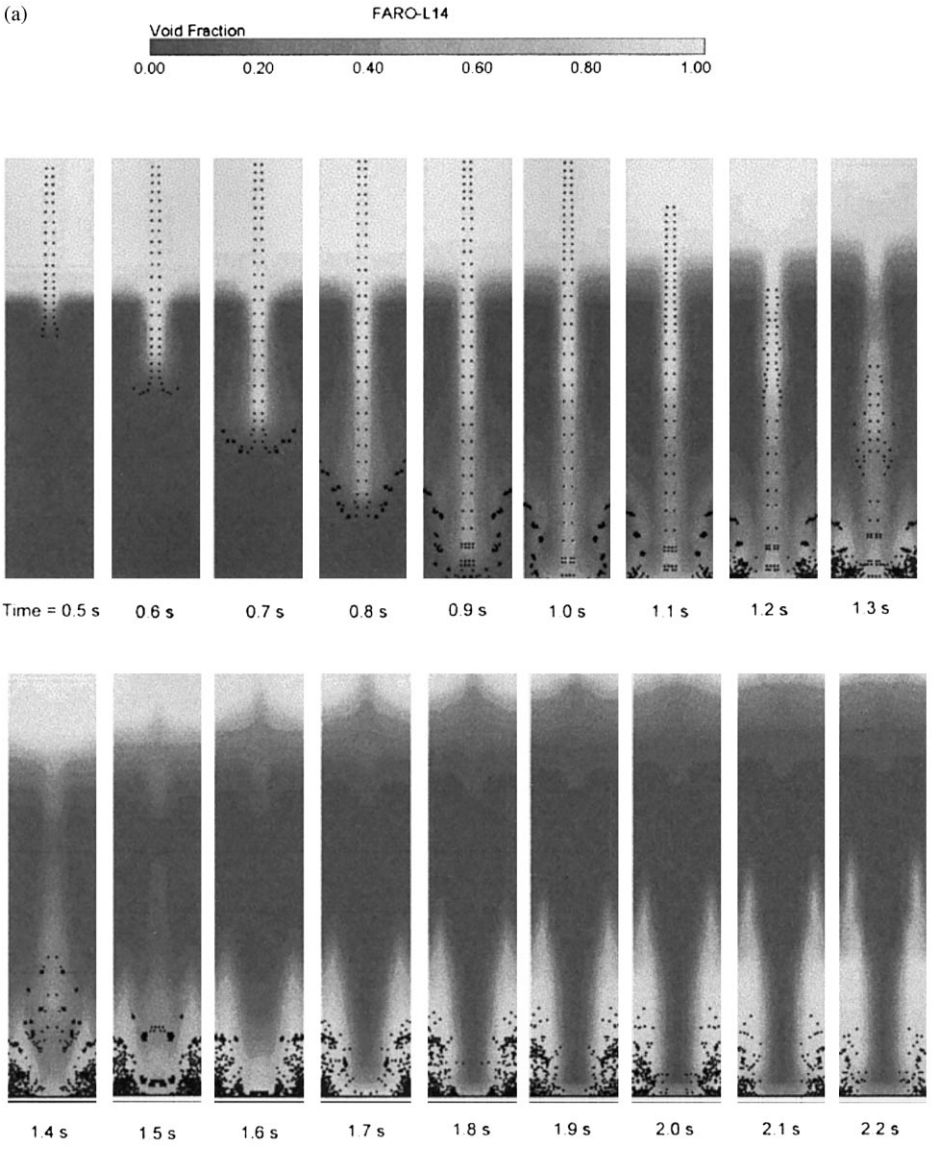

Fig. 52. (a). The calculated transient mixing behavior of FARO L-14. (b) The calculated transient mixing behavior of FARO L-19.

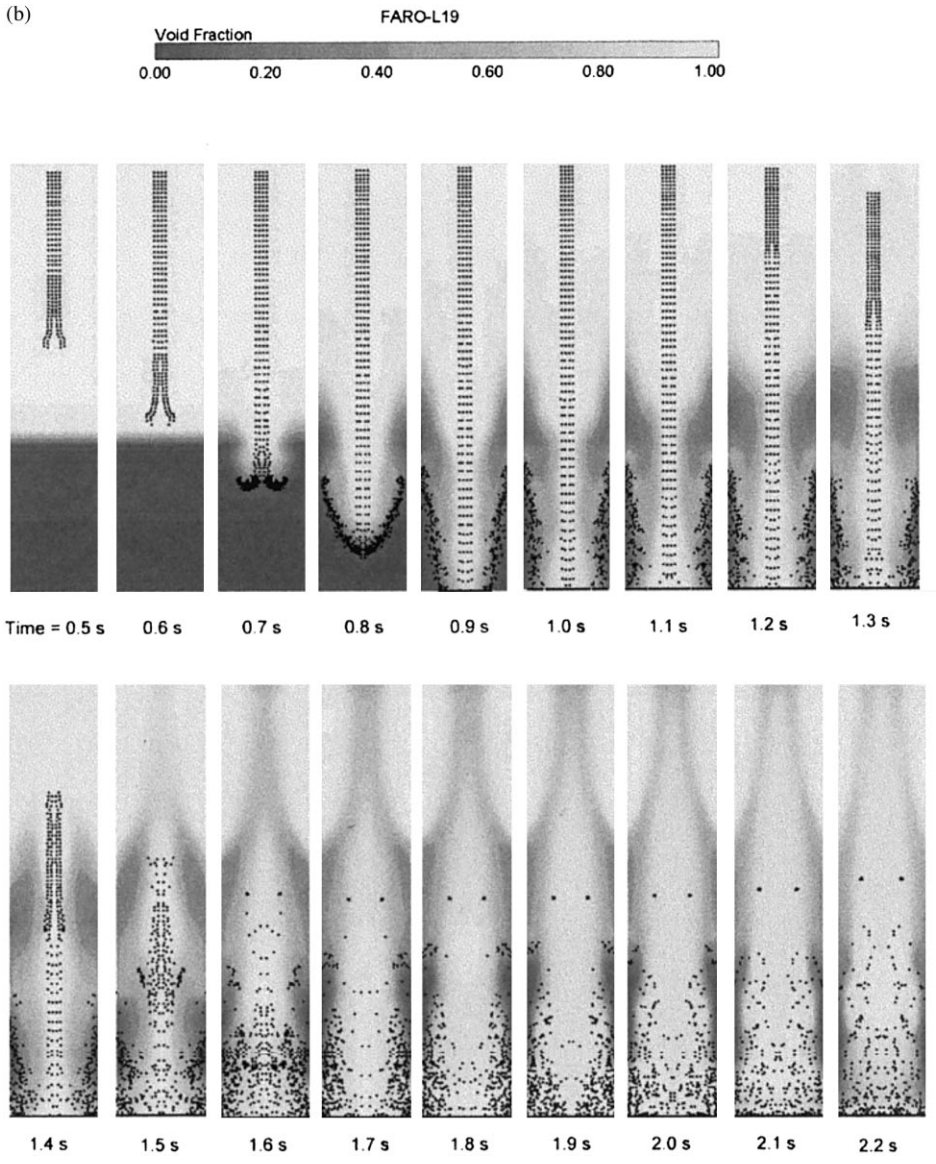

Fig. 52. (*Continued*)

of which 83.5 MJ was estimated to transfer into water/steam. In L-14, the corresponding heat transfers at the end of 1.4 s were estimated to be 35.2 and 37.2 MJ, respectively. These results are in general agreement with the numerical data presented in Fig. 56.

The thermocouple traces are shown in Figs. 57 and 58, in comparison with predicted histories of liquid, vapor and saturation temperatures at respective locations. Also, we show the predicted local melt and liquid volume fractions, as to convey the local regime, potential for superheating the gas and wetting the thermocouples, which would then show the saturation temperature. For high enough liquid fractions these measurements should transit to the actual liquid temperature. These comparisons read in conjunction with the flow regimes in Fig. 52a,b, not only show good

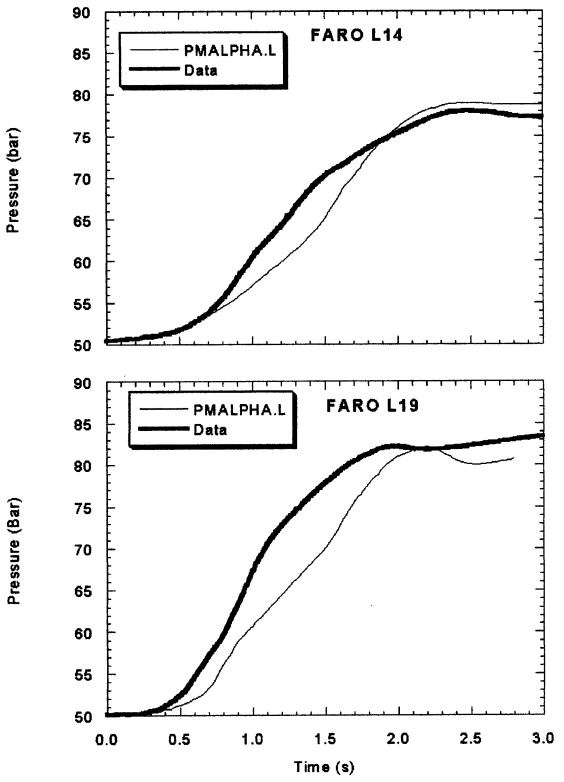

Fig. 53. Comparison between the calculated pressure history and experimental data for FARO L-14 and 19.

agreement with the temperature measurements but also provide substantial support for the inference made through the computations on the regimes of interaction. Except in regions where there were obvious breakdowns of the thermocouples due to the presence of high temperature melt (mainly along the center line), the agreement between measurements and predictions is excellent. In L- 14, the temperature along the boundary and at the upper part of the pool ($r \geq 0.15$ m, $z \geq 1$ m) shows excellent agreement with the predicted liquid temperature, it being substantially below the predicted saturation temperature. This is consistent with the predicted pool behavior as depicted in Fig. 52a. The 'interaction' between the melt and water at the lower half of the pool causes the upper part to rise as a 'liquid slug', compressing the steam above it. The corresponding temperature measurements, in the same positions for L-19, on the other hand, agree with the predicted saturation temperature which is consistent with the prediction of large void fraction along the pool boundary.

Finally, in Figs. 59 and 60, we show the debris masses, as function of time and the debris spectra at the end, for runs L-14 and 19, respectively. In the calculation, fuel breakup is terminated either when the fuel is more than 50% frozen or when the fuel particle diameter is less than 2 mm. Fuel which can no longer be broken up is considered as the debris mass. The comparison of debris size distribution is thus meaningful only for $D_p > 2$ mm. As shown in Figs. 59 and 60, the agreement is generally good. In the experiment, a fraction of the debris mass collected after the test is identified as 'cake' (20 and 60 kg for L-14 and 19, respectively). These are masses which are stabilized by external freezing prior to being broken up into 'fine' debris with small diameters—they would tend to merge together into a 'cake' once collected at the pool bottom. To correlate the predicted

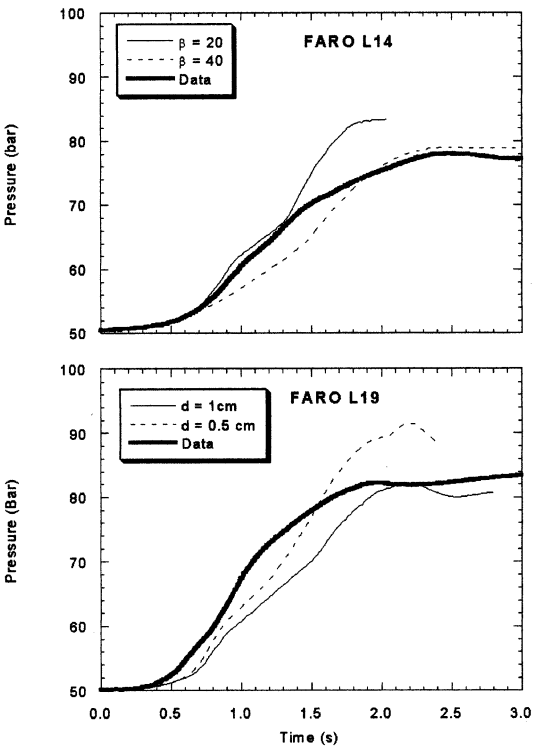

Fig. 54. Predicted parametric behavior of the calculated pressure history for FARO L-14 and 19.

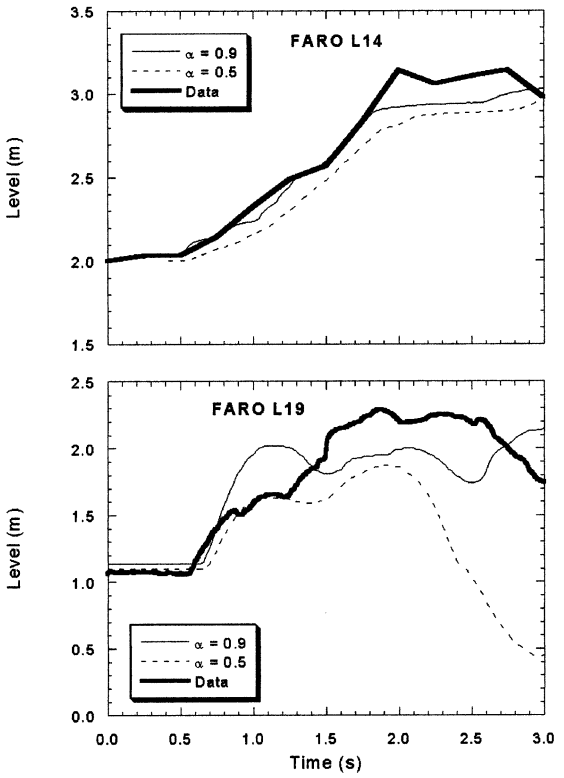

Fig. 55. Comparison between the calculated level swell history and experimental data for FARO L-14 and 19.

debris mass with this experimental observation, the predicted debris mass with 'large' diameter ($D_p > 9$ mm) are plotted together with the total debris mass in Figs. 59 and 60. The mass of the 'large' diameter debris are predicted to be 25 and 35 kg for L-14 and 19, respectively. Even though the exact definition of 'large' debris ($D_p > 9$ mm) is uncertain, this agreement shows that PM-ALPHA.L consistently captures the relevant breakup behavior for the FARO tests.

4. Breakup aspects

Consideration of breakup *directly* in a verification effort is hampered by the lack of experimental data on the dynamics of the process. In single jet experiments, one can approximately determine the position of complete disintegration, but no information is available for the breakup processes above, or the extent of further breakup below this point. The closer the melt approaches the molten corium conditions, the more intense is the interaction and even less information of breakup dynamics becomes possible. Of course, one has the end state, by means of the solidified debris (although some ambiguities even here are possible by merging of semisolidified particles) and this may be used as one anchor, which together with measured interactions parameters, such as steaming rates, pressurization and level swell, can be used to *back out* the dynamics of breakup (as we have done for the MIXA and FARO tests). Clearly, however, this is susceptible to the code's performance in the multifield aspects (hence our attention to them) and, moreover, it is open to question whether the *same model* of breakup can capture the behavior from one test to another and eventually in reactor conditions. The size and melt masses of FARO

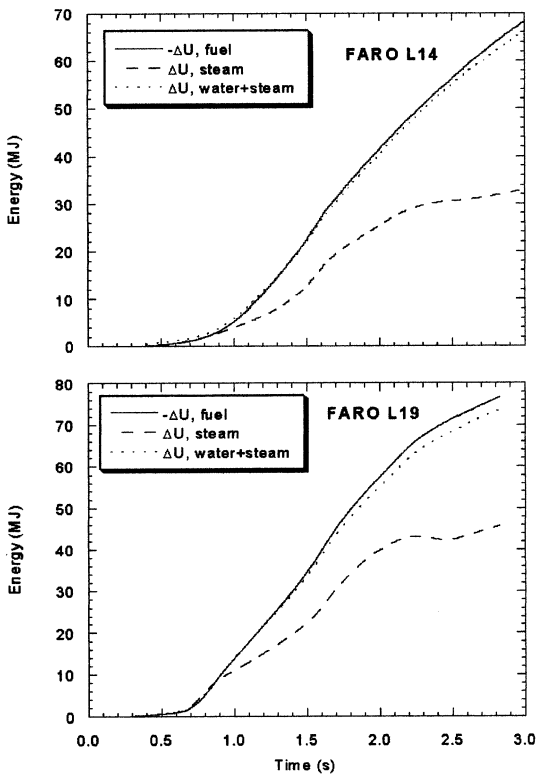

Fig. 56. Predicted energy partition for FARO L-14 and 19.

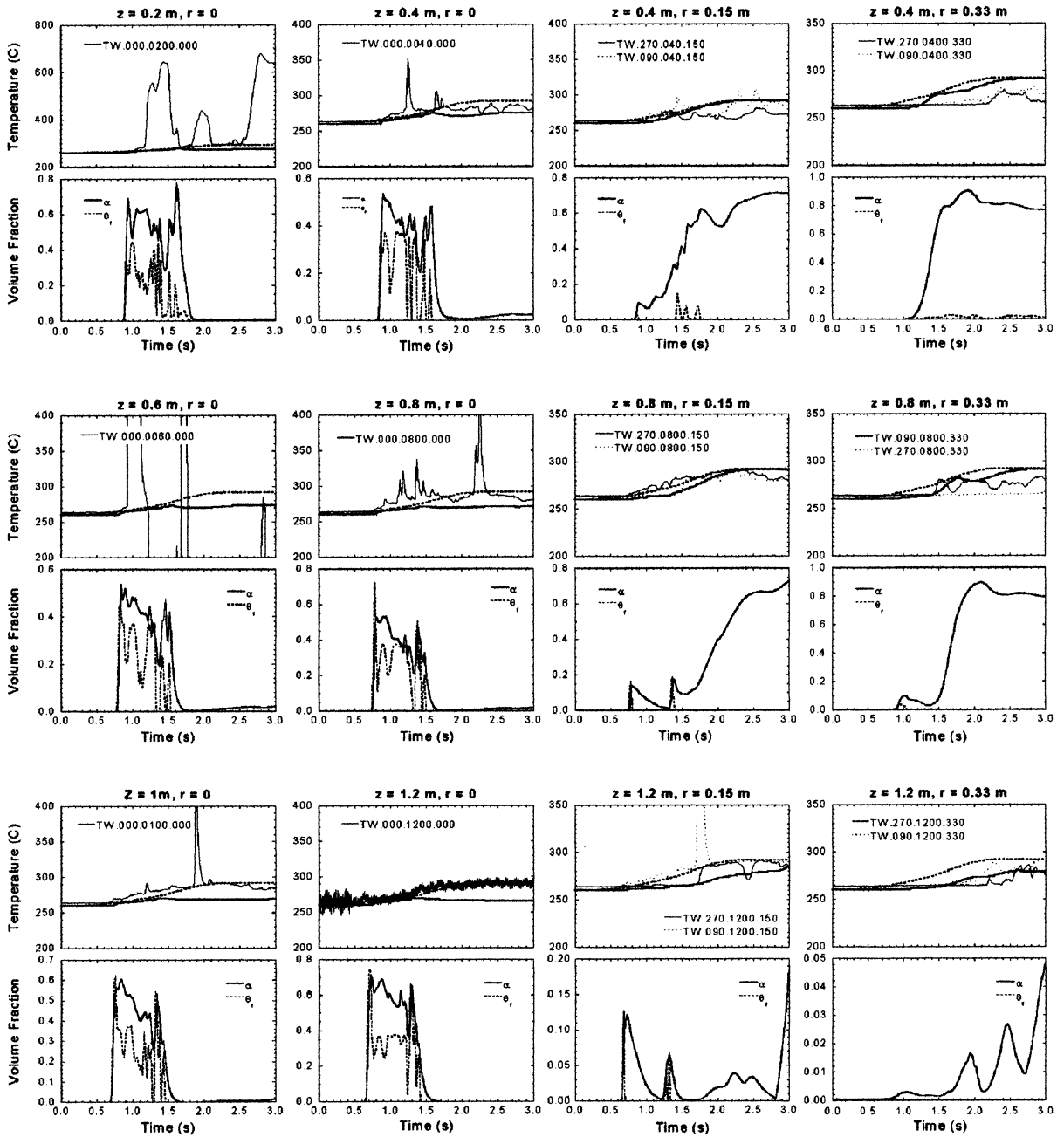

Fig. 57. Calculated and measured liquid temperature transient for FARO L-14. Each pair of figures (lined up vertically) represent temperature (top figure), fuel volume fraction and void fraction (bottom figure) predicted on a specific location (indicated on the top figure) by PM-ALPHA.L. Temperature data are also presented in the top figure. The dark solid and dashed lines on the top figures correspond to the calculated liquid and saturated temperature, respectively.

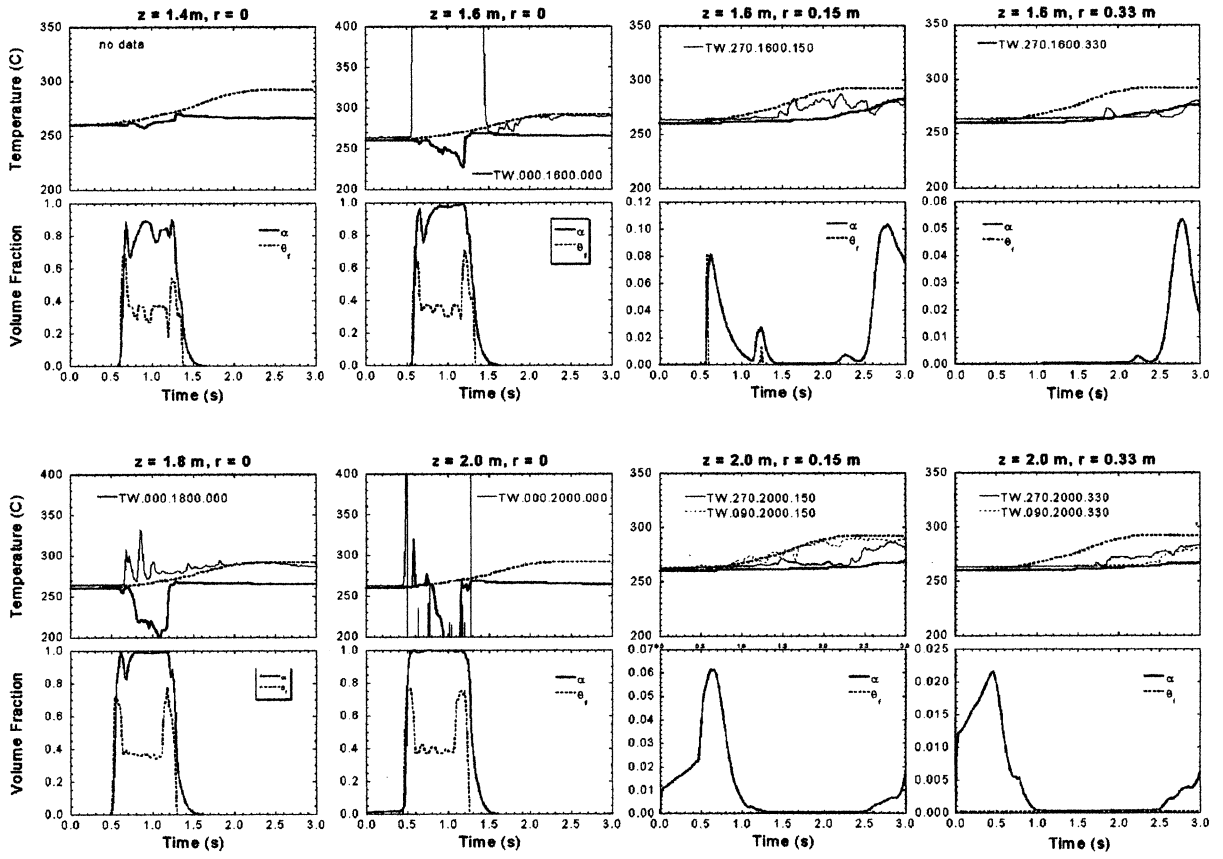

Fig. 57. (*Continued*)

are helpful in accepting an empirical approach based on it and the planned lower pressure tests will be of further help. Meanwhile, we can use the MIXA tests which indicate that lower pressures promote breakup (higher steam velocities snowballing in combination with breakup). Thus, in combination, the two tests and their above interpretations with PM-ALPHA, provide reasonable choices of parameters to bound the breakup behavior for reactor calculations.

Another avenue, complementary to the above, would involve deep investigations (both experimental and theoretical) on the fundamentals along the lines currently pursued by detailed jet and drop breakup models (Kondo et al., 1993; Bürger et al., 1995; Chu et al., 1995).

5. Numerical aspects

5.1. Space/time discretization

With available computing power and the usual limited lateral dimensions of melt pours, we can go down to cm-scale nodes, even for 3D representation. Thus, for premixing, we see no representation (accuracy) issues due to discretization. With respect to time discretization, we have found the proper domains to obtain robust and accurate computations and this has not been a problem.

5.2. Numerical diffusion

Numerical diffusion is always present, but we have found that in premixing calculations it can

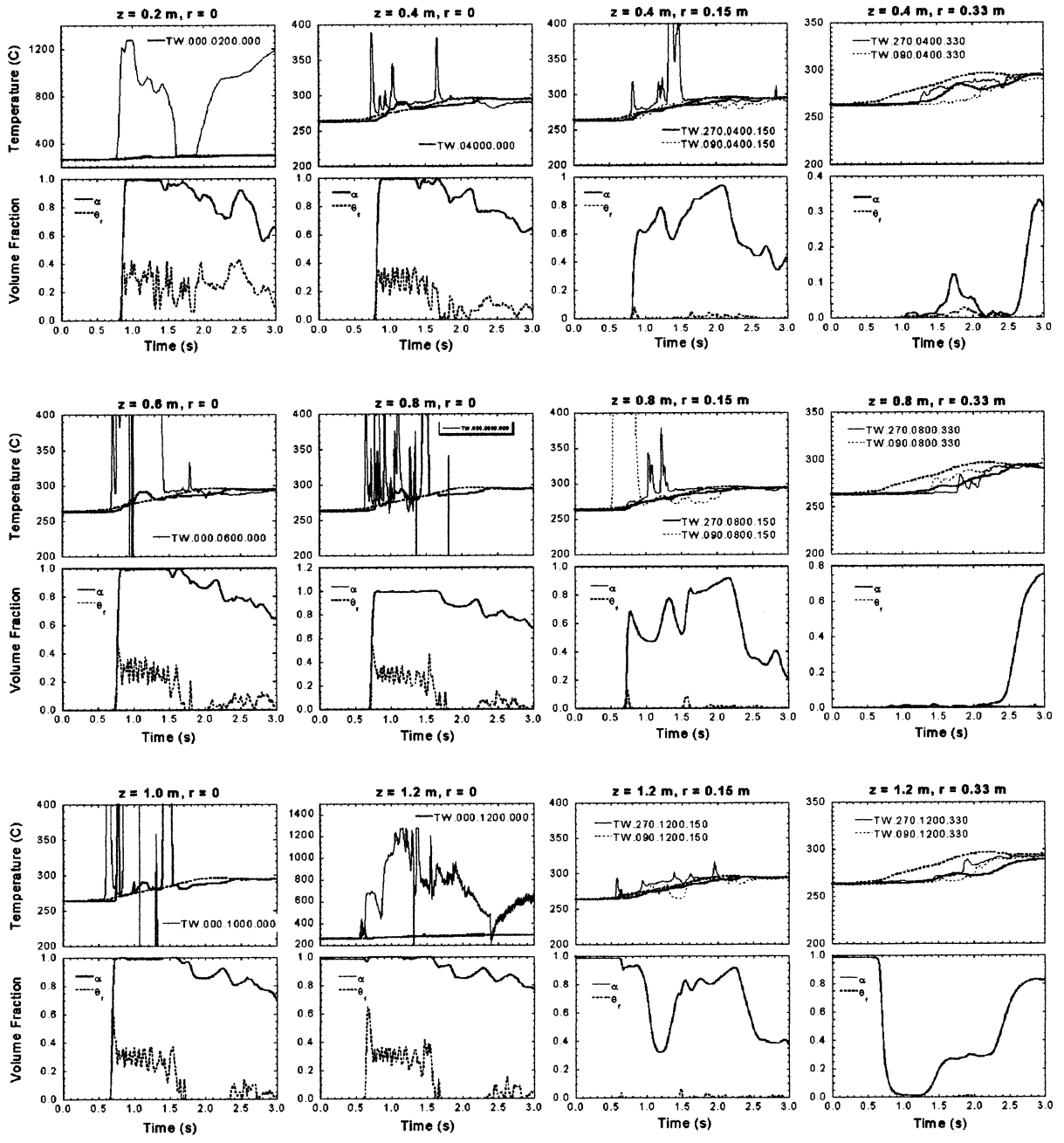

Fig. 58. Calculated and measured liquid temperature transient for FARO L-19. Each pair of figures (lined up vertically) represent temperature (top figure), fuel volume fraction and void fraction (bottom figure) predicted on a specific location (indicated on the top figure) by PM-ALPHA.L. Temperature data are also presented in the top figure. The dark solid and dashed lines on the top figures correspond to the calculated liquid and saturated temperature, respectively.

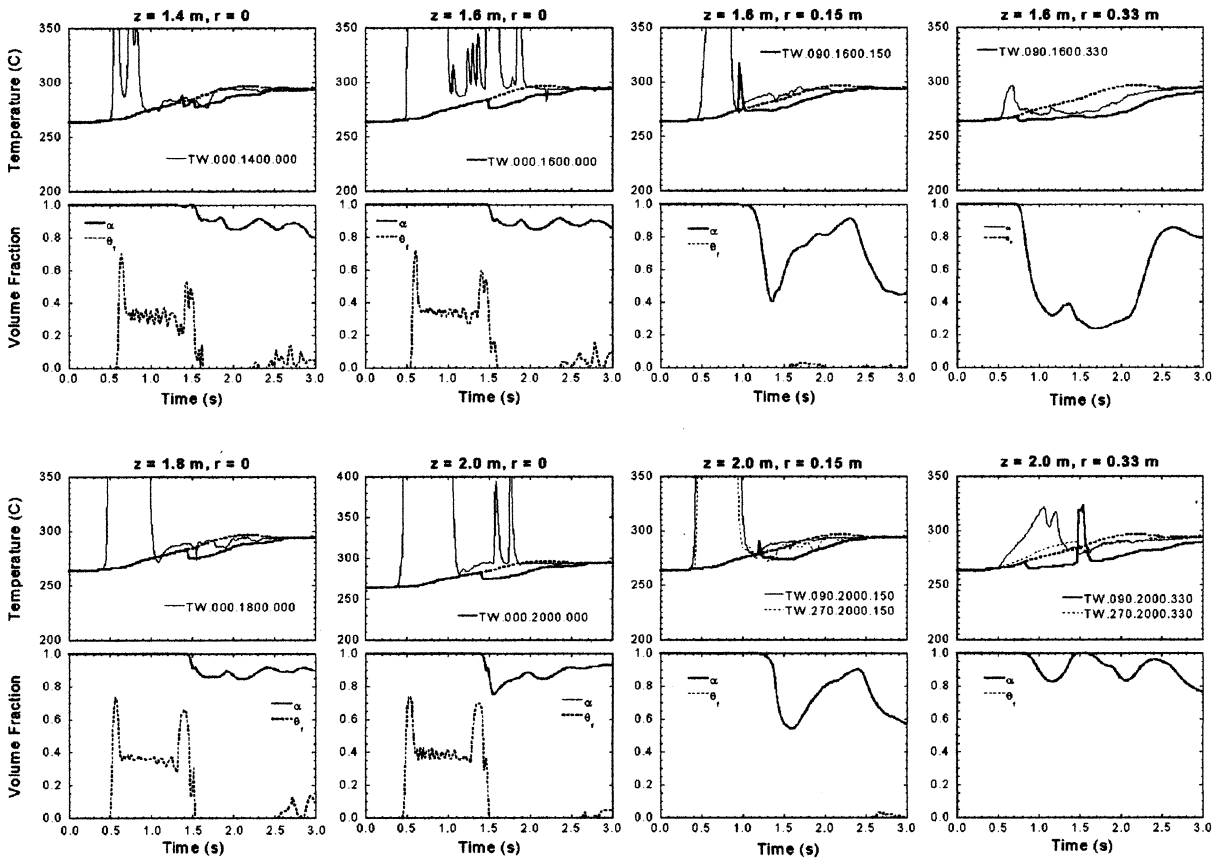

Fig. 58. (*Continued*)

be largely controlled by the use of an adequately fine computational grid. Still, some inappropriate melt diffusion at the front is inevitable and the associated feedback on the dynamics (void formation, etc.) could be questioned. Thus we arrived finally to PM-ALPHA.L and are quite satisfied that it has eliminated this problem.

6. Concluding remarks

In this verification effort, we have tried to provide an in-depth testing of the multifield aspects of the PM-ALPHA code. On the numerical side we see no major outstanding issues. On the physical side, further attention is needed on constitutive laws for breakup. However, the results presented here indicate that actual behavior can be represented quite well with reasonable choices of the breakup parameter β and cutoffs due to high void, solidification and Weber number criteria. Moreover, this experience provides useful guides for bounding the behavior, as it is our approach for reactor calculations. As discussed in Appendix A of DOE/ID-10504 and as demonstrated by the first integral application (DOE/ID-10541), this bounding task is of reasonable proportions mainly because of the compensating effects between voiding, particle size and solidification, on energetics.

Acknowledgements

This work was supported under the ROAAM program carried out for the US DOEs Advanced

Reactor Severe Accident Program (ARSAP), under ANL subcontract No. 23572401 to UCSB.

Appendix A

In the analysis of the two QUEOS runs with high steaming rates (Q17 and 34), the modeling of the 5 m vent line of the facility and the interpretation (timing relative to pressure in the vessel) of the flow measurement in it (2.5 m from the inlet) are extremely important for a quantitative comparison between the prediction from PM-ALPHA.L and experimental data. For example, we found major differences between the quoted value of losses in this pipe and what is apparent from

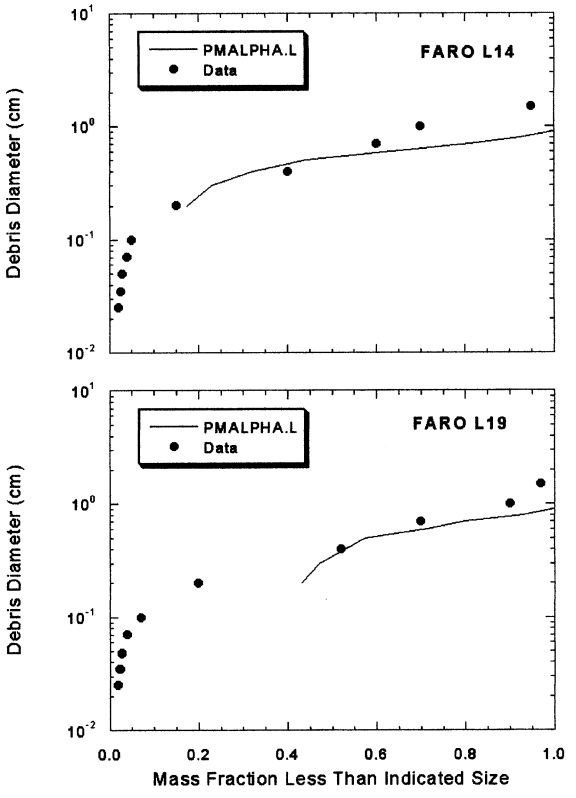

Fig. 59. Comparison between the calculated debris mass and its size distribution and experimental data for FARO L-14.

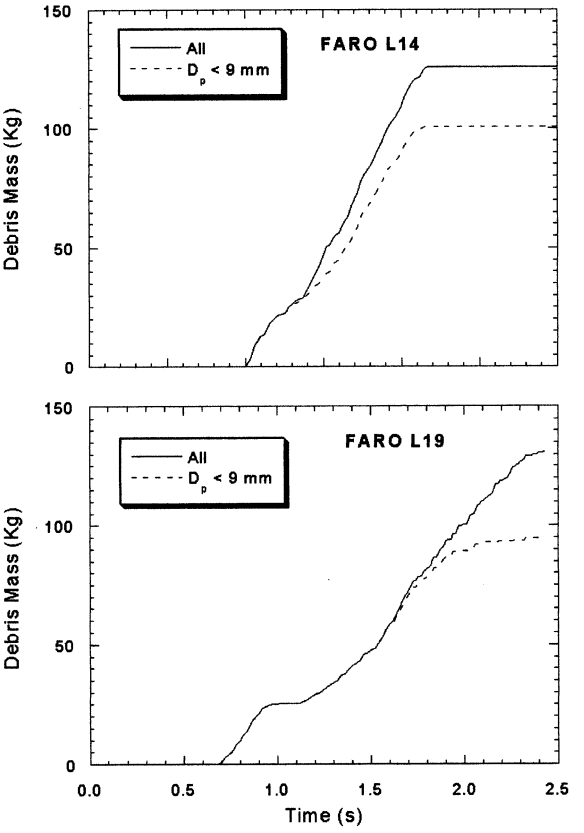

Fig. 60. Comparison between the calculated debris mass and its size distribution and experimental data for FARO L-19.

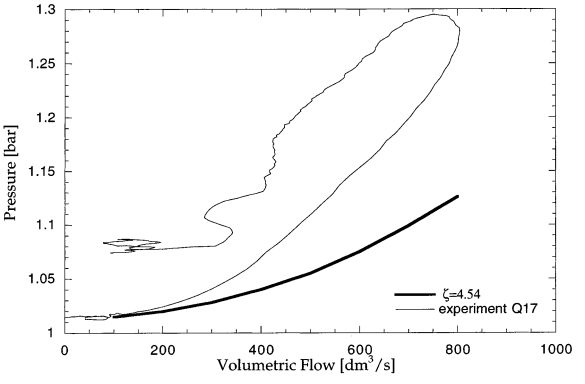

Fig. 61. Trajectories of measured flow rates and pressure drops in the QUEOS vent line for run Q17. Also shown is a calculated trajectory based on the loss factor quoted in the QUEOS test report—it was measured in independent experiments using a steady flow of air.

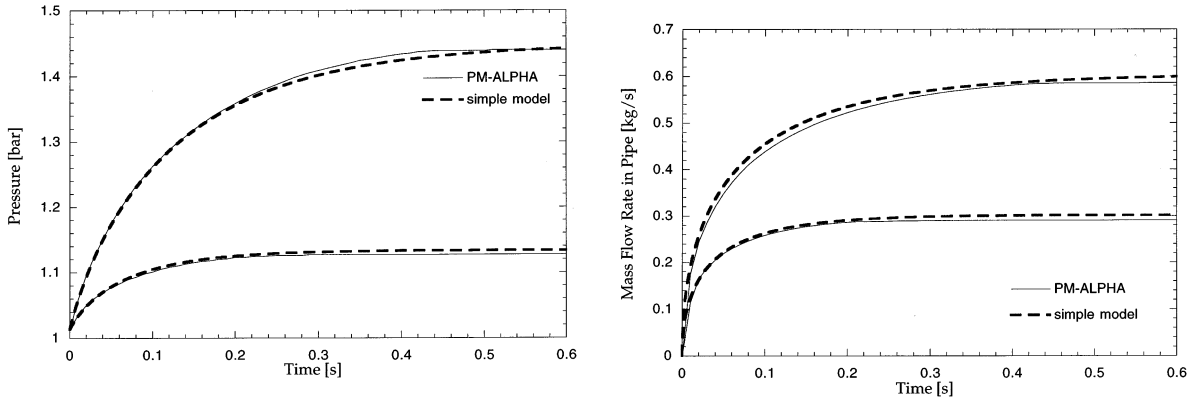

Fig. 62. The transient response of the QUEOS vessel-vent line system under a steady steam flow supply of 0.5 and 1 $m^3\ s^{-1}$.

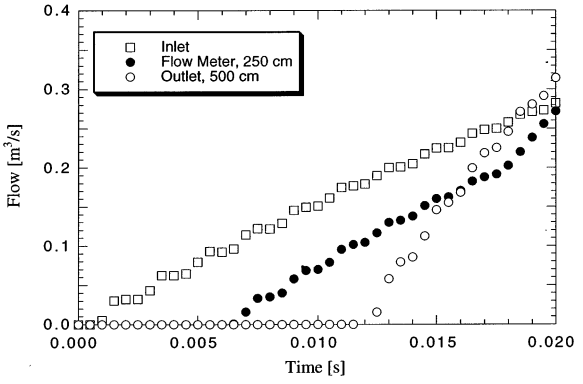

Fig. 63. Illustration of the delay time in the pressure-flow signals due to the length of the vent line and location of the flow meter in it.

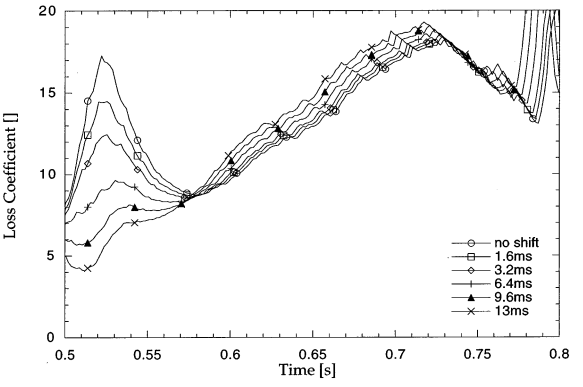

Fig. 65. The loss factor behavior in Q17, extracted according to Eq. (A5), with the delay time, t^*, as a parameter.

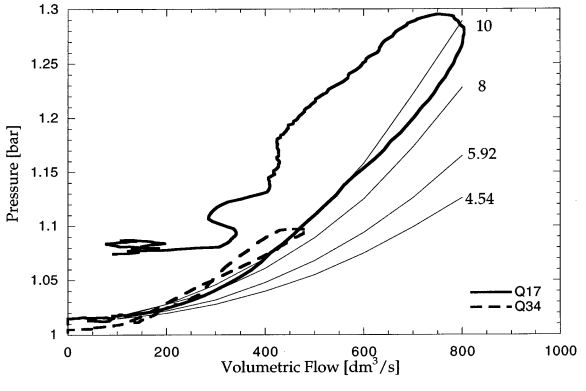

Fig. 64. The loss factor behavior of the QUEOS vent line for the two tests considered.

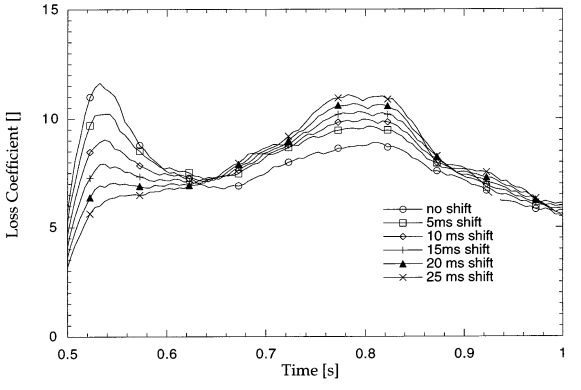

Fig. 66. The loss factor behavior in Q34, extracted according to Eq. (A5), with the delay time, t^*, as a parameter.

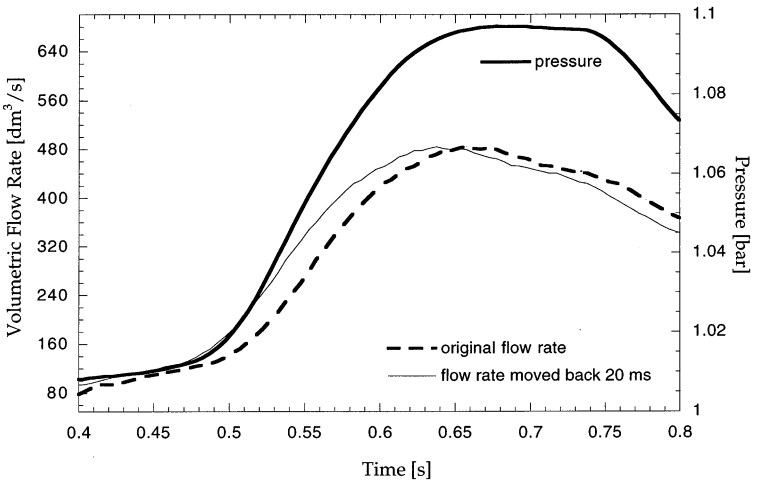

Fig. 67. Illustration of the time shift required for 'synchronization' of the pressure-flow data in Q34.

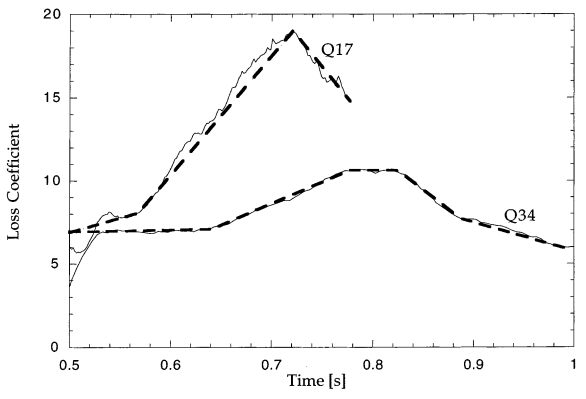

Fig. 68. Deduced loss factors (transient behavior) from runs Q17 and 34.

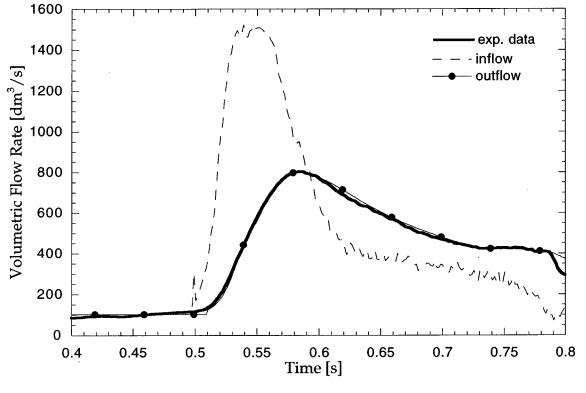

Fig. 69. The inlet flow required to produce the measured flow (in the vent line) in Q17.

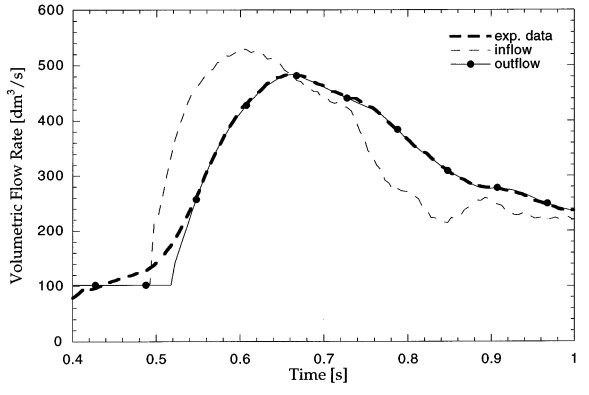

Fig. 70. The inlet flow required to produce the measured flow (in the vent line) in Q34.

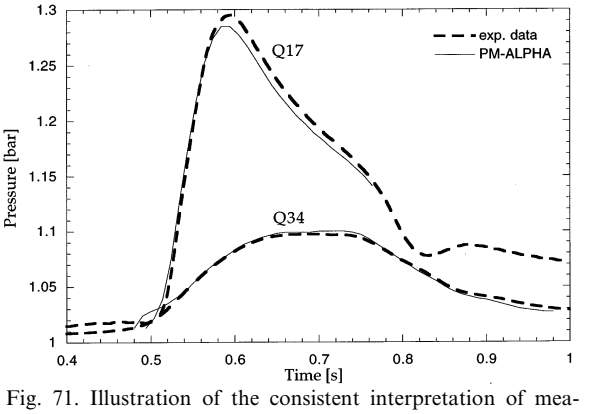

Fig. 71. Illustration of the consistent interpretation of measured pressure transients in Q17 and 34. The code was driven by the inlet flow in Figs. 69 and 70, respectively and the loss factors in Fig. 68.

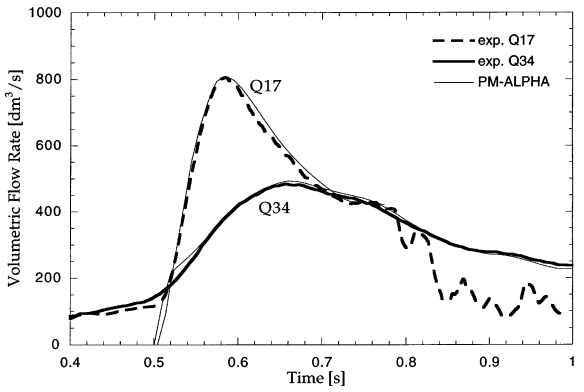

Fig. 72. Illustration of the consistent interpretation of measured flow transients in Q17 and 34. The code was driven by the inlet flow in Figs. 69 and 70, respectively and the loss factors in Fig. 68.

the actual data (see Fig. 61) In this appendix we describe our approach to this problem. It consisted of the following four steps.

A.1. Step 1

Determine and understand the roles of the freeboard volume and vent line loss factor, under constant steam production rate and gain experience with PM-ALPHA in representing these.

Neglecting temperature changes we have an exact solution for the pressure history, given by

$$0.5\frac{t}{\tau} = -\sqrt{\frac{P-P_0}{\frac{\xi\rho_e}{2}\left(v_i\frac{A_i}{A_e}\right)^2}} - \ln\left(1-\sqrt{\frac{P-P_0}{\frac{\xi\rho_e}{2}\left(v_i\frac{A_i}{A_e}\right)^2}}\right) \quad \text{(A1)}$$

where the time constant τ is given by

$$\tau = \frac{\xi}{2}\frac{\rho_e V Q_i}{P_e A_e^2} \quad \text{(A2)}$$

and Q_i is the inlet flow rate, V is the freeboard volume, P_e and ρ_e are pressure and density at the exit (atmospheric), A_e is the exit flow area and ξ is the total pipe loss factor. From these we can obtain the flow rate transient by

$$Q_e = A_e\sqrt{\frac{2(P-P_e)}{\rho_0\xi}} \quad \text{(A3)}$$

Results for a loss factor of 10 (see below for this choice) and two inlet flow rates, 0.5 and 1 $m^3\ s^{-1}$, corresponding to the peak flows in the two tests considered here, are shown in Fig. 62. These figures also show PM-ALPHA.L results, with a vent pipe of 50 cm and the loss factor distributed over three computational cells within the pipe. In Fig. 63, we can see the effect of the pipe length in introducing a time delay in the flow transient measured, as in the QUEOS tests, 2.5 m away from the inlet.

A.2. Step 2

Understand the loss factor behavior in the experiments.

The measured pressure-flow trajectories in the two experiments considered here are shown in Fig. 64. In the experiment, the major losses were upstream of the flow meter and the frictional losses of the pipe itself were negligible, so the $\Delta P - \dot{Q}_e$ data pairs shown in Fig. 64 should be consistent (save for some time delay to be discussed shortly) to an overall loss factor representation such that

$$\Delta P = \frac{1}{2}\xi\rho_e\frac{\dot{Q}_e^2}{A_e^2} \quad \text{(A4)}$$

where subscript e signifies exit (atmospheric) conditions. Constant ξ lines of this equation are also shown in Fig. 64 and indicate that the portions of the experimental trajectories that correspond to the rising flow rate portions of the transients are characterized by loss factors between 8 and 10. These are significantly higher than the 4.54 value quoted by the experimenters (obtained from separate, steady, air-blow experiments). More importantly, the decaying portions show still higher and non-reproducible values, with Q17 reaching $\xi \sim 20$!

We can imagine two potential reasons for this apparent increase in pipe losses *during* the experiments: water entrainment and carryover into the pipe; and condensation on pipe walls and flow straightener, upstream of the flow meter. Water entrainment is certainly evident within the field of view of the video frames (the upper region of the freeboard space and entrance to the vent pipe are

not shown) and is consistent with the much greater buildup of losses in Q17 that had considerably more intense interaction. Condensation is possibly a significant cause also, because even if initially at saturation temperature, pipe walls and internals would become subcooled as pressure increased through the transient. In fact, there are indications (i.e. thermocouple reading inside vent pipe) that there might have been subcooling even to begin with. Precise estimates must account for mixing with the air initially present (unknown quantity) and its effect in impeding condensation. Recognizing that these details are quite peripheral to our subject and that with the limited information available on them further elaboration would quickly be met by limited returns, *further consideration of the QUEOS experiments requires us to*

1. *assume* that condensation did not play an important role and
2. deduce an empirical representation of the pipe loss factor variation with time and use it as a boundary condition in our PM-ALPHA.L simulations.

In fact, even item (2) is not as straightforward as one might first imagine as discussed next.

A.3. Step 3

Extract, empirically, the loss factors in the experiments.

As noted in Step 1, due to the large (2.5 m) distance of the flow meter from the interaction vessel, the pressure and flow readings are not 'physically synchronous', as required in the definition of an overall loss factor. This would not create a problem if we were to simulate, in PM-ALPHA.L, the whole vent line and take the flow predicted at the position of the flow meter for comparison. However, given the 'problems' with the loss factor variation with time noted above this would be unnecessarily cumbersome. Rather, we introduce a constant delay, t^*, in the flow measurement to extract the loss factor, by

$$\xi = \frac{2(P(t) - P_e)A_e^2}{\rho_e \dot{Q}_e^2(t + t^*)} \tag{A5}$$

Plotted in this fashion for different values of t^*, the experiment $\Delta P - \dot{Q}_e$ data for Q17 and 34 are shown in Figs. 65 and 66, respectively. As expected, we find that a delay of ~ 6–15 ms is necessary to obtain a reasonable behavior in the loss factor in the early portion of the transient. This is consistent with the entrainment explanation—it would be expected to build with time, leaving a nearly constant value of the loss factor initially and with a value closer to the 4.54 value measured with air under steady conditions. Note that this does not include the entrance losses (from the vessel to the pipe) present in the experiment. Also note that at the very start of the transient (the first ~ 20 ms) both flows and pressures are very low, so that measurement errors propagate to a rather large uncertainty in the loss factor. Some small amounts of condensation may further add to this early uncertainty, but both effects would be expected to diminish (in relative terms) with time as flow and pressure build up, leaving entrainment the dominant factor. The appropriateness of time delay so deduced is also confirmed by the illustration in Fig. 67. As a conclusion of this analysis we will use the time-wise variation of the pipe loss factors, for these two runs, as shown in Fig. 68.

A.4. Step 4

Demonstrate the consistent reproduction of the experimental pressure and flow rate transients with PM-ALPHA.L and determine the *inlet* flow transients needed to produce these behaviors.

The needed flow rate transients are obtained by the simple model, that led to Eqs. (A1), (A2) and (A3), applied in differential time increments together with the loss factors shown in Fig. 68. The results are shown in Figs. 69 and 70. Remarkable is the vapor generation 'pulse' needed to produce the measured *flow* and *pressur*e transients in Q17. For the milder Q34, the difference between input and measured flows is much less, but still significant. Finally, using these input flow transients in PM-ALPHA.L, together with the loss factors in Fig. 68 we could reproduce, consistently, the measured pressure and flow transients, as shown in Figs. 71 and 72, respectively. It should be noted

that the slightly smaller (10 versus 10.8 cm) pipe diameter in PM-ALPHA.L, imposed by the 5 cm node size selected for discretization, was taken into account; scaling by a factor of 0.735 is needed.

References

Angelini, S., Yuen, W.W., Theofanous, T.G., 1993. Premixing-related behavior of steam explosions. In: Proceedings CSNI Specialists Meeting on Fuel-Coolant Interactions, Santa Barbara, CA, 5–8 January 1993, NUREG/CP-0127, March 1994, pp. 99–133. (See also Nucl. Eng. Design 155 (1995) 115–157).

Angelini, S., Theofanous, T.G., Yuen ,W.W., 1995. The Mixing of Particle Clouds Plunging Into Water, NURETH-7, Saratoga Springs, NY, 10–15 September, NUREG/CP-0142, vol. 1, pp. 1754–1778

Angelini, S., Theofanous, T.G., Yuen, W.W., 1997. On the Regimes of Premixing. In: OECD/CSNI Specialist Meeting on Fuel-Coolant Interactions, Jaeri, Tokai, Japan, 19–21 May. (Also this issue of NED).

Bürger, M., Berg, E.v., Buck, M., Fichter, U., Schatz, A., 1995. Fragmentation and Film Boiling as Fundamentals in Premixing, US–Japan Joint Seminar: A Multidisciplinary International Seminar on Intense Multiphase Interactions, Santa Barbara, CA, 9–13 June, pp. 29–55.

Chu, C.C., Sienicki, J.J., Spencer, B.W., 1995. Validation of the THIRMAL-1 melt-water interaction code. In: Proceedings of the Seventh International Meeting of Nuclear Reactor Thermal-Hydraulics (NURETH-7), Saratoga Springs, NY, 10–15 September, vol. 3, pp. 2359–2384.

Denham, M.K., Tyler, A.P., Fletcher, D.F., 1992. Experiments on the mixing of molten uranium dioxide with water and initial comparisons with CHYMES code calculations. In: Proceedings of the Fifth International Topical Meeting On Reactor Thermal Hydraulics (NURETH-5), Salt Lake City, UT, 21–24 September, pp. 1667–1675.

Fletcher, D.F., 1992. A comparison of coarse mixing predictions obtained from the CHYMES and PM-ALPHA models. Nucl. Eng. Design 135 (1992), 419–425.

Fletcher, D.F., Denham, M.K., 1993. Validation of the CHYMES mixing model. In: Proceedings CSNI Specialists Meeting on Fuel-Coolant Interactions, Santa Barbara, CA, 5–8 January 1993, NUREG/CP-0127, March, pp. 89–98.

Fletcher, D.F., 1995. Multiphase mixing: some modeling questions. In: International Symposium on Two-Phase Flow Modeling and Experimentation, Rome, Italy, October.

Hanratty, T.J., Bandukwala, A., 1957. Fluidization and sedimentation of spherical particles. AIChE J. 3, 293–296.

Hibbit, H.D., et al., 1994. ABAQUS Version 5.3.

James, R.J., 1989. ANACAP-3D—Three-dimensional analysis of concrete structures: theory, user's and verification manuals, ANATECH No. ANA-89-0094.

Kondo, Sa., Konishi, K., Morita, K., Shitakawa, N., Furutani, A., 1993. Fuel-coolant interactions studies at PNC relevant to fast reactor safety. In: International Seminar on Physics of Vapor Explosion, Tomakomai, Hokkaido, Japan, 25–29 October, pp. 96–109.

Magallon, D., Hohmann, H., 1995. Experimental investigation of 150 kg scale corium melt jet quenching in water. In: Proceedings of the Seventh International Meeting on Nuclear Reactor Thermal-Hydraulics (NURETH-7), Saratoga Springs, NY, 10–15 September, pp. 1688–1711.

Magallon, D., Leva, G., 1996. FARO LWR Programme-Test L-14 Report, Technical Note No. 1.96.25, Joint Research Centre, ISPRA, January.

Meyer, L., 1996. The interaction of a falling mass of hot spheres with water. In: ANS Proceeding of the 1996 National Heat Transfer Conference, Houston, TX, August, pp. 105–114.

Meyer, L., Schumacher, G., 1996. QUEOS, a Simulation-Experiment of the Premixing Phase of a Steam Explosion with Hot Spheres in Water, FZKA Report 5612, Forschungszentrum Karlsruhe, April.

Richardson, J.F., Zaki, W.N., 1954. Sedimentation and fluidization: part I. Trans. Inst. Chem. Eng. 32, 35–53.

Theofanous, T.G., 1996. On the proper formulation of safety goals and assessment of safety margins for rare and high-consequence hazards. Reliability Eng. Syst. Safety 54, 243–257.

Theofanous, T.G., Yuen, W.W., 1993. The probability of alpha-mode containment failure updated. In: Proceedings CSNI Specialists Meeting on Fuel-Coolant Interactions, Santa Barbara, CA, 5–8 January, NUREG/CP-0127, March 1994, pp. 331–342.

Theofanous, T.G., Yuen, W.W., Angelini, S., Chen, X., 1995. The Study of Steam Explosions in Nuclear Systems, DOE/ID-10489, January.

Theofanous, T.G., Yuen, W.W., Angelini, S., 1998a. Premixing of steam explosions: PM-ALPHA verification studies, DOE/ID-10504, June.

Theofanous, T.G., Yuen, W.W., Freeman, K., Chen, X., 1998b, Escalation and propagation of steam explosions: ESPROSE.m verification studies, DOE/ID-10503, June.

Theofanous, T.G., Yuen, W.W., Angelini, S., 1998. The internal dynamic structures of a class of transient dispersed flows with phase change. In: Third International Conference on Multiphase Flow, 8–12 June, Lyon, France.

THIRMAL-1, 1993. Computer code for analysis of interactions between a stream of molten corium and a water pool, vol. 1: Code Manual, EPRI TR-103417-V1, Project 3130-01, Final Report (December 1993), vol. 2: User's Manual, EPRI TR-103417-V2, Project 3130-01, Final Report (December 1993).

Wallis, G.B., 1969. One-Dimensional Two-Phase Flow. McGraw-Hill, New York.

Yuen, W.W., Theofanous, T.G., 1995a. PM-ALPHA: A Computer Code for Addressing the Premixing of Steam Explosions, DOE/ID-10502, May.

Yuen, W.W., Theofanous, T.G., 1995b. ESPROSE.m: A computer code for addressing the escalation/propagation of steam explosions. DOE/ID-10501, April.